Optical and Thermodynamic Analysis and Optimization of a Novel Solar Concentrating System for Distributed Power Generation

A THESIS
SUBMITTED TO THE FACULTY OF THE GRADUATE SCHOOL
OF THE UNIVERSITY OF MINNESOTA
BY

Marc Tyler Deo Dunham

IN PARTIAL FULFILLMENT OF THE REQUIREMENTS
FOR THE DEGREE OF
MASTER OF SCIENCE

Advised by Professor Wojciech Lipiński

August 2012

Acknowledgements

Many thanks to Dr. Vipin Kumar and Dr. Shyam Boriah of the Computer Science department, for always making me feel welcome in the PSI group and allowing me the freedom to contribute my own ideas.

Thank you to Dr. Anoop Mathur and Dr. Rajan Kassetty of Terrafore, Inc., who provided financial support for a portion of my studies and whose research proposal helped contribute to a significant portion of this work.

To the dedicated instructors, particularly Professor Terry Simon, Professor John Bischof, and Professor Frank Kelso of the Mechanical Engineering department, who have helped me develop a strong work ethic and passion for learning.

Thank you to Dr. Brian Iverson at Sandia National Laboratories, for your invaluable comments on everything solar.

Thanks to Lindsey Yue of the Solar Group, for sharing your frustrations and listening to mine.

Thank you to my parents, who have always supported my endeavors and helped instill in me the value of education.

Last but certainly not least, I want to express my deepest and most sincere thanks to my adviser, Professor Wojciech Lipinski, for giving me the guidance to be successful in graduate study. Your faith in my abilities, even (and especially) during rough times, kept me on track and believing in myself. Through dozens of painstaking paper iterations and re-writes I have become a competent technical writer, and I could not have done it without your steady help.

Dedication

This thesis is dedicated to my wife Carly, who put up with ridiculous work schedules, innumerable panic attacks (some quite serious), and long technical commentary, all with such grace and strength to reaffirm my belief in myself, my dreams, and my potential to change the world. I would not be writing this thesis or looking to the future with such hope if it were not for you, and I am continually amazed by the person you have helped me to become. Also to Kai, who gives me a fresh perspective on learning and inspires me to be a better teacher and student. I hope this work can inspire you some day.

Abstract

A novel central receiver power system is analyzed for distributed-scale concentrated solar power. The Monte Carlo ray tracing technique is used to characterize the optical performance of a linked-tracking heliostat field. The design point parameters are found through parametric optimization, and annual simulations are carried out for five different heliostat linkage configurations. Smaller linkage groupings are typically found to have a lower impact on performance, with a 1x2 linkage causing a maximum system efficiency reduction of 1.64% in December, and a 5x5 linkage causing a 29.5% reduction. The results of the optical analysis are then used as inputs to a thermodynamic analysis of heat engine power cycles. In all cases the concentrated flux drives a Brayton cycle operating with air, CO_2, He, or H_2. A combined Brayton–Rankine cycle is also considered with bottoming fluids C6-Fluoroketone, cyclohexane, HFE-7000, n-Pentane, R-141b, and R-245fa. Average 7-hour daily efficiencies are calculated for each month. The maximum daily average solar-to-electric conversion efficiency is calculated to be 16.2% with a single CO_2 Brayton cycle and a 1 (east-west) x 2 (north-south) linkage setup. A peak system conversion efficiency of 18.2% was calculated when using R-141b as the working fluid in a bottoming cycle.

Table of Contents

List of Tables

List of Figures

Nomenclature

A_{rec}	receiver aperture area (m^2)
A_{launch}	solar ray launch area (m^2)
A_{ref}	single reflector aperture area (m^2)
AM	air mass
C	solar flux concentration ratio
d	distance (m)
E	energy (J)
F	factor
G_0	solar constant ($W\text{-}m^{-2}$)
h	mass-specific enthalpy ($kJ\text{-}kg^{-1}$)
$h_{altitude}$	height above sea level (m)
h_{post}	length of reflector post (m)
h_{rot}	length of rotation arm (m)
h_{tilt}	length of tilt arm (m)
I_D	direct solar radiation ($W\text{-}m^{-2}$)
i	row number
j	column number
$\dot{m}$	mass flow rate ($kg\text{-}s^{-1}$)
$\hat{\mathbf{n}}$	unit normal vector
N	number
P	power (W)
p	pressure (MPa)
$\dot{Q}$	heat rate (W)
$\dot{Q}''_{rec}$	heat flux at the receiver ($W\text{-}m^{-2}$)
$\vec{r}$	position vector
R	radius (m)
$\Re$	random number
s	mass-specific entropy ($kJ\text{-}kg^{-1}\text{-}K^{-1}$)
$\hat{\mathbf{s}}$	directional unit vector
t	time (s)
$\hat{\mathbf{t}}$	orthogonal unit vector
T	temperature (K)
w_{ref}	reflector width (m)
W	mass-specific work ($kJ\text{-}kg^{-1}$)
$\dot{W}$	mechanical power (W)

Greek

α	absorptivity
α_{solar}	solar altitude angle (deg)
β	tilt angle (deg)
δ	declination angle (deg)
ε	emissivity
ε_{reg}	Brayton cycle regenerator effectiveness
η	efficiency
γ	azimuthal angle (deg)
ω	hour angle (deg)
φ	rotation angle (deg)
ϕ	latitude angle (deg)
σ	Stefan-Boltzmann constant, 5.670E-8 W-m^{-2}-K^{-4}
$\sigma_{optical}$	standard deviation of optical error
τ	transmissivity
θ	polar angle (deg)

Subscripts

base	base of reflector post
blocking	relating to blocking
bottom	relating to the bottoming Rankine cycle
center	center of object
combined	relating to the combined cycle
compressor	relating to the Brayton cycle compressor
cost	relating to cost
deviation	relating to a deviation from ideal behavior
ground	relating to the ground plane
int	intercept
launch	relating to the solar ray launch region
max	maximum
min	minimum
modified	relating to a modified angle due to deviation
net	output minus input
optical	relating to the optical concentrator
pinch	relating to the pinch point in the combined cycle heat exchanger
R	ratio
ray	relating to a single stochastic ray

rec	relating to the receiver
ref	relating to a reflector
reflection	relating to reflection
s	isentropic
shading	relating to shading
shaft	relating to the Brayton cycle turbine-compressor shaft
solar	relating to solar rays
spillage	relating to reflected radiation captured by receiver
system	relating to the optical-thermodynamic system
tangent	relating to a tangent vector
th	thermal
top	topping or single Brayton cycle
turbine	relating to the Brayton or Rankine cycle turbine
useful	absorbed by receiver
zenith	relative to the zenith direction

Abbreviations

CC	Component Cost
CSP	Concentrated Solar Power
HDR	Heliostat-to-Drive Ratio
HEX	Heat Exchanger

Chapter 1. Introduction

The use of concentrated solar power (CSP) has been explored for large-scale power generation as a means of electric power and thermal energy conversion since the 1970s [1–3]. By implementing a large reflector area which focuses incident sunlight onto a small receiver area, a very high heat flux at a target point can be attained. This high heat flux is typically aimed at an absorber surface, which can reach high temperatures depending on the magnitude of impinging heat flux, the absorber's design, and the method of heat removal. High temperature heat obtained in the solar absorber can be used to drive thermodynamic or thermochemical processes [4]. The prospect of electric power generation from concentrated solar radiation is particularly attractive as the fuel, sunlight, is free and abundant. Furthermore, there are no harmful emissions as with fossil fuel plants, no potential for toxic byproducts as with nuclear power plants, and construction can have a smaller impact on the surrounding environment than other renewables such as hydroelectricity. Interest in CSP as an alternative to conventional power generation techniques has intensified in recent years most notably due to economic concerns over projected fossil fuel shortages and environmental concerns over the increase of harmful emissions into the atmosphere [4,5]. However, the study of CSP involves a complex set of systems, each of which must be optimized in order to compete with more established technologies.

The first component in a CSP system is the optical concentrating unit. As the concentrator provides the first opportunity for performance loss in the system, it is critical

that it be designed efficiently. Different types of solar concentrators have been extensively studied and reported on in the literature [1,4,6]. For applications demanding medium-to-high temperatures for process heat and electric power generation, optical systems with the ability to deliver solar concentration ratios above 50 suns (50 kW/m^2) are typically required. Roughly in order of increasing solar concentration ratio delivery, four primary technologies have emerged which are commonly used to meet high-temperature demands with CSP: linear Fresnel reflectors (LFR), parabolic trough concentrators (PTC), heliostat field concentrators (HFC), and parabolic dish collectors (PDC) [4,6]. These technologies are compared by a few general metrics in Table 1.

Table 1. Major solar concentrating technologies for high-temperature processes compared by a few key metrics.

Technology	Relative Maturity [4]	Relative Cost [4]	Typical Concentration Ratios	Typical Uses
LFR	Mature	Low	10–100	Process heat
PTC	Most mature	Very low	10–100	Process heat, electricity
HFC	Most recent	High	300–1500	Thermochemical process heat, electricity
PDC	Recent	Very high	500–2000+	Electricity

The next step in the solar thermal conversion process is absorption of concentrated sunlight by a solar receiver, which accepts the concentrated solar flux from the optical concentrator and converts it to high-temperature heat which may be used for sensible water heating or driving a thermodynamic cycle. While not treated extensively in this

thesis, a brief discussion of solar receivers is warranted here as they represent a critical component of any CSP system. The design of receivers varies widely by application, the type of concentrator system used, and the type of heat transfer process required. For linear concentration systems such as PTC and LFR, tubular absorbers are commonly used [6,7]. In this type of receiver, solar flux is concentrated along a focal line where the linear absorber is placed. Typically a heat transfer or working fluid is heated in the tube by the concentrated solar flux. Historically most linear concentration systems have used unpressurized oils or other heat transfer fluids in the absorber which then are passed through a heat exchanger to heat the working fluid, usually steam, for a heat engine cycle [6,7]. However, more recently the idea of directly heating a pressurized working fluid in the linear absorber has been considered. Pressurized steam has been shown to be viable in direct heating systems, offering higher thermal efficiencies as the need for an intermediary heat exchange process is eliminated. However, concerns are present regarding the safety of running high pressure steam along great tube lengths [7].

In PDC systems, a small engine/receiver combination is commonly placed at the focal point of a parabolic dish and is fixed to the structure to maintain its position during tracking operations. The most common type of engine is the Stirling engine, inside which pistons or rotary drives are moved by expansion and compression of a gas. Helium has been a favorable choice for Stirling engine working fluids due to its good heat transfer characteristics [8]. Hydrogen has excellent heat transfer characteristics and has shown very high efficiency in solar dish-Stirling configurations [9], but raises concerns because

of its flammability and the fact that it is more difficult to seal the chambers.

For HFC systems, an array of heliostat reflectors concentrates solar flux onto a central receiver device. The central receiver passes heat to a heat-to-electric conversion system or heat exchanger by way of an absorber. HFC systems are usually utilized for electric power generation, typically through a heat engine run by a working fluid. The working fluid can either be heated directly in tubes or panels [1,3,10] or while flowing through a porous media/volumetric receiver [11–14], or indirectly by a heat transfer fluid such as molten salt [15,16]. A system utilizing molten salt or other thermal mass is more resistant to transients and may provide storage, but greatly complicates the design and limits the operating conditions due to the required heat exchange process and material limitations of the storage medium.

Steam Rankine cycles are often used for PTC, LFR, and HFC systems [4,6,7,10]. Rankine cycles utilizing organic working fluids, referred to as Organic Rankine Cycles (ORC), have been used to process heat in lower flux systems due to their favorable performance at lower temperatures and power ratings when compared to steam Rankine cycles [17,18]. Stirling engines run using expanding and compressing gases in a piston or rotary engine. They typically have high efficiencies but are limited in size and are expensive to implement [6]. Brayton engines have been gaining attention for use in CSP systems because of their scalability and affordability compared to Stirling engines. In addition to being used for HFC and possibly PTC or LFR systems, Brayton cycle microturbines have the potential to encroach on Stirling engine technology’s use in PDC

configurations because of lower production costs from established industry [6].

1.1. Distributed solar power generation

There has been interest in using CSP technology in a distributed-scale manner, most notably in urban rooftop applications, small district heat and power style supply, or for small community power generation off the grid [6,19,20]. Interest has been shown in developing CSP-related technologies on a reduced scale which supports the pursuit of distributed-scale CSP applications. On the concentration side, small mirrors have been shown to be effective in two-axis tracking systems, reducing complexity and expense when compared with large bulky heliostats [21,22]. Because of their small size they can also be manufactured with higher precision, reducing specular error and increasing performance [23]. Gas microturbines have been proposed for other industries to generate low-output power and heat (< 500 kW_e) at moderate thermal efficiencies (~20–30%) [24–27]. Gas microturbine component efficiencies offer a substantial benefit at low power ratings to steam turbine components, for which the isentropic turbine efficiency can drop to as low as 25–50% in the 10–500 kW_e power range [17,18]. Lower power outputs are inevitably an intrinsic characteristic of distributed-scale systems, making gas microturbines a very attractive option both in terms of the performance benefit vs. steam turbines and the cost benefit vs. Stirling engines.

1.2. Objective

This thesis focuses on a new approach to a distributed-scale central receiver CSP system. The design uses small mirrors and a novel mechanically-linked sun tracking system designed to decrease the complexity and cost of the optical concentration component, which typically accounts for about 50% of initial system costs [3,4]. Monte Carlo ray tracing is a common way to analyze solar concentrating systems [3,21,22,28,29]. Due to the unique nature of the tracking linkage, an in-house Monte Carlo ray tracing program is developed and used for the analysis. Concentration ratios, power delivery, and optical efficiency are observed parametrically on the summer solstice and an optimized set of parameters is simulated for each month of the year using five different linked tracking configurations and compared to the case of individual heliostat tracking. Results are then coupled with a thermodynamic simulation of multiple heat engine power cycle configurations carried out in Engineering Equation Solver [30].

Chapter 2. Problem Statement

The system to be analyzed includes an optical concentrator, a solar receiver, and a heat engine realizing a thermodynamic cycle, with the focus of analysis being primarily the optical and thermodynamic aspects. The model system is shown in Fig. 1.

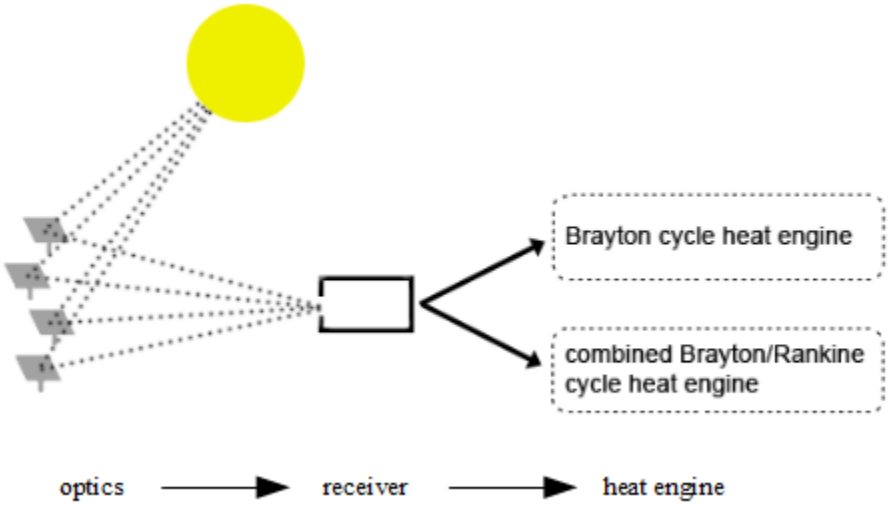

Fig. 1. Diagram of CSP system to be analyzed.

The optical system consists of a field of spherical mirrors with square aperture area, and a central receiver. The optical field is visualized in Fig. 2.

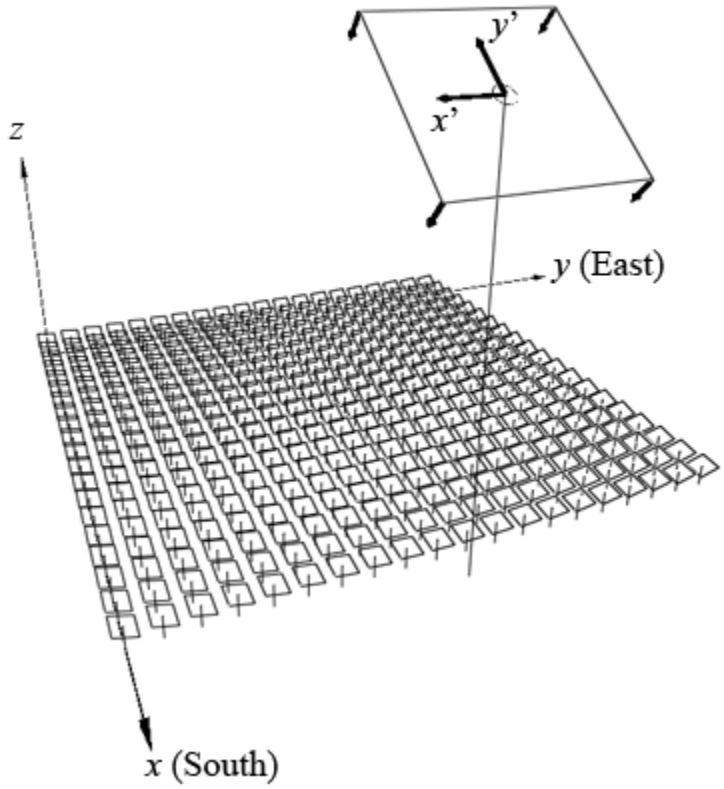

Fig. 2. Optical concentrating system showing local coordinates of the field (*x*,*y*,*z*) and of the receiver plane (*x*',*y*').

Sunlight strikes the field of mirrors and is focused in the receiver plane. The concentrated radiation is converted to high-temperature heat, which is then transferred in the solar receiver to the working fluid of a thermodynamic cycle. Specific parameters are varied to optimize the performance of the optical concentrator. The relevant design point parameters for the optical system are outlined in Table 2.

Table 2. Optical concentrator design point parameters found through optimization procedures.

Parameter	Value
Reflector width (w_{ref})	0.8 m
Optimum mirror curvature radius to focal length ratio	2.0
Receiver position ($r_{rec,z}$)	17.5 m
Grid spacing ($d_{spacing}$)	$1.4w_{ref}$
Optical error ($\sigma_{optical}$)	3.5 mrad
Receiver radius (R_{rec})	0.35 m

The primary thermodynamic cycle driven by the receiver is a Brayton cycle, utilizing gas microturbine technology. A combined cycle is also considered, in which heat normally rejected to the ambient by the Brayton cycle is used to drive a low-temperature Organic Rankine Cycle (ORC). Electric generators may be connected to the cycles to produce electric power. The effect of linking heliostats together by common sun-tracking drives on the overall system performance is examined through coupled analyses of the optics and thermodynamic cycles.

Chapter 3. Optics

In order to determine the inputs to the thermodynamic analysis, the performance of the optical concentrating system must be characterized. This is done by defining the field geometry, the solar model, and performing Monte Carlo ray tracing analyses.

3.1. Concentrator geometry

The heliostats are arranged in a square grid as illustrated 3-dimensionally in Fig. 2 and in an overhead view in Fig. 3.

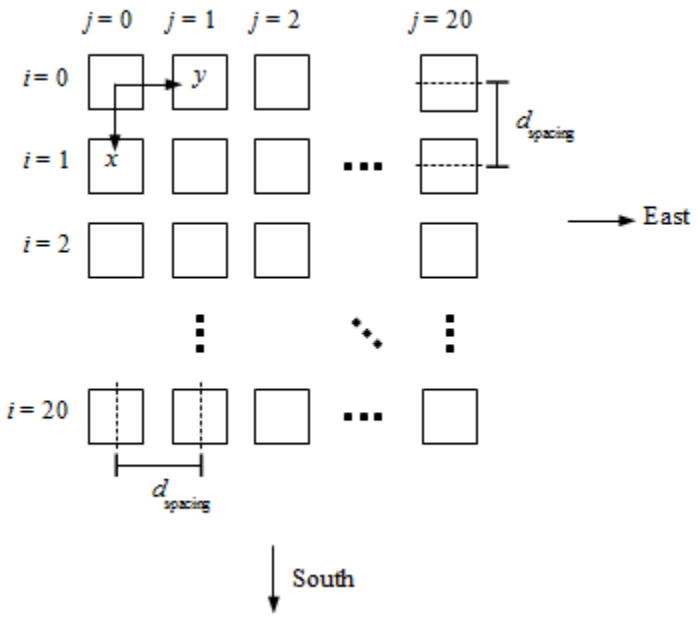

Fig. 3. Overhead view of heliostat grid arrangement.

The receiver center is located at the south end of the field, with a position defined by:

$$\vec{r}_{\text{rec,center}} = \left(N_{\text{rows}}\right) d_{\text{spacing}}\,\hat{\mathbf{i}} + \frac{\left(N_{\text{columns}} - 1\right)}{2} d_{\text{spacing}}\,\hat{\mathbf{j}} + r_{\text{rec,center,z}}\,\hat{\mathbf{k}} \qquad (1)$$

The vertical position of the receiver center is varied parametrically in the analysis. The heliostats have a range of motion so that they can effectively reflect solar radiation to the receiver as the sun's position changes. The range of motion of an individual heliostat is given in Fig. 5.

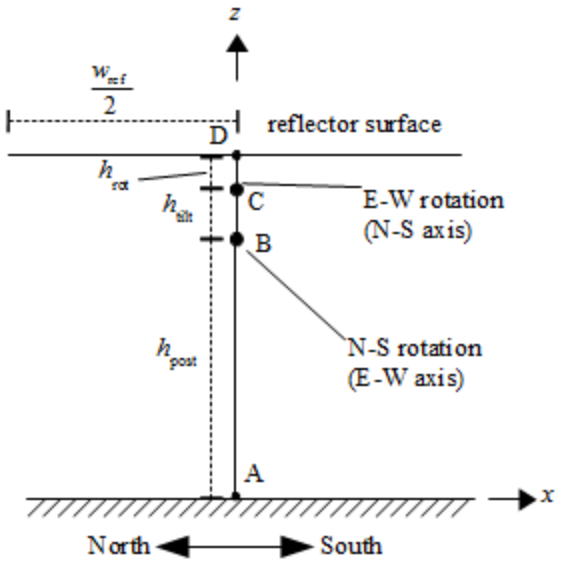

Fig. 4. Schematic of individual heliostat.

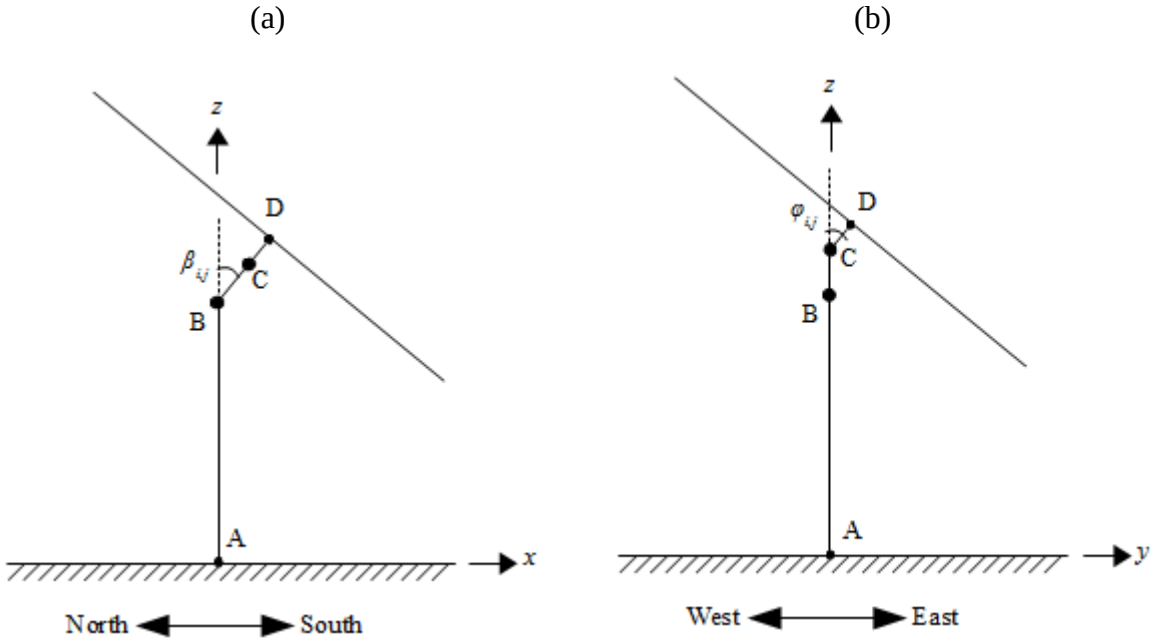

Fig. 5. (a) range of tilt motion in the north–south direction, and (b) range of rotational motion in the east–west direction.

There are two independent angular velocities used in tracking: one with a north-south tilt axis and one with an east-west tilt axis. The direction north-south tilt axis varies between horizontal (true north-south) and vertical, while the east-west axis always runs horizontally. The basic construction of an individual reflector is shown in Fig. 5a. Each reflector is mounted on a fixed base point A, to which the reflector is connected through a support and tracking mechanism. The reflector post AB is oriented vertically in the z-direction and fixed to the ground at point A with no rotational freedom. The tracking linkage is free to rotate about the east-west axis at point B and about the north-south axis at point C, and is affixed to the reflector at point D. The rotational freedom of the reflector is illustrated in Fig. 5a and b. The angle $\beta_{i,j}$ is the north-south tilt measured

between the segment BC and the vertical post for a heliostat at grid coordinates *i*,*j*, and $\varphi_{i,j}$ is the angle of east-west rotation measured between segment CD and a line extending from segment BC, with positive angles tilting toward the east and negative values toward the west. The base position of each reflector, point A in Fig. 5, is defined by:

$$\vec{r}_{\text{ref,base},i,j} = (i-1)\,d_{\text{spacing}}\,\hat{\mathbf{i}} + (j-1)\,d_{\text{spacing}}\,\hat{\mathbf{j}} + 0\hat{\mathbf{k}} \tag{2}$$

The center of the reflector, point D in Fig. 5, is defined by:

$$\begin{aligned}\vec{r}_{\text{ref,center},i,j} = \vec{r}_{\text{ref,base},i,j} &+ \left(h_{\text{tilt}}\sin\left(\beta_{\text{i,j}}\right) + h_{\text{rot}}\sin\left(\beta_{\text{i,j}}\right)\cos\left(\phi_{\text{i,j}}\right)\right)\hat{\mathbf{i}} \\ &+ \left(h_{\text{rot}}\sin\left(\phi_{\text{i,j}}\right)\right)\hat{\mathbf{j}} \\ &+ \left(h_{\text{post}} + h_{\text{tilt}}\cos\left(\beta_{\text{i,j}}\right) + h_{\text{rot}}\cos\left(\beta_{\text{i,j}}\right)\cos\left(\phi_{\text{i,j}}\right)\right)\hat{\mathbf{k}}\end{aligned} \tag{3}$$

The unit normal of the reflector at the center of the receiver is defined by:

$$\begin{aligned}\hat{\mathbf{n}}_{\text{ref,center},i,j} = &\sin\left(\beta_{\text{i,j}}\right)\cos\left(\phi_{\text{i,j}}\right)\hat{\mathbf{i}} \\ &+ \sin\left(\phi_{\text{i,j}}\right)\hat{\mathbf{j}} \\ &+ \cos\left(\beta_{\text{i,j}}\right)\cos\left(\phi_{\text{i,j}}\right)\hat{\mathbf{k}}\end{aligned} \tag{4}$$

3.2 - The solar model

As the results of the entire simulation depend on knowing the direction of solar rays at any given time, a model must be used. A schematic of the geometric relations used to define the direction of solar rays is given in Fig. 6.

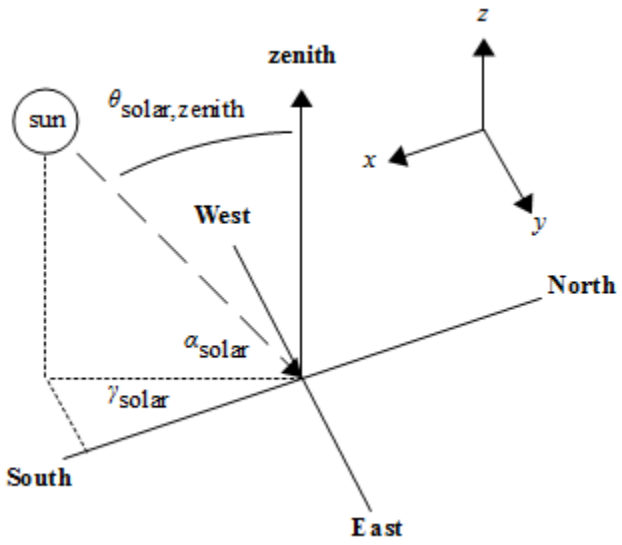

Fig. 6. Geometric representation of quantities used in solar position modeling.

Developing relations from Fig. 6, the unit vector of a solar ray originating at the center of the solar disc is computed as:

$$\hat{\mathbf{s}}_{\text{solar,center}} = -\cos\alpha_{\text{solar}}\cos\gamma_{\text{solar}}\hat{\mathbf{i}} + \cos\alpha_{\text{solar}}\sin\gamma_{\text{solar}}\hat{\mathbf{j}} - \sin\alpha_{\text{solar}}\hat{\mathbf{k}} \tag{5}$$

where the solar altitude and azimuth angles, α_{solar} and γ_{solar}, respectively, are given by [31]:

$$\alpha_{\text{solar}} = \frac{\pi}{2} - \theta_{\text{solar,zenith}} \tag{6a}$$

$$\cos\theta_{\text{solar,zenith}} = \cos\phi\cos\delta\cos\omega + \sin\phi\sin\delta \tag{6b}$$

$$\gamma_{\text{solar}} = \text{sign}(\omega)\left|\cos^{-1}\left(\frac{\cos\theta_{\text{solar,zenith}}\sin\phi - \sin\delta}{\sin\theta_{\text{solar,zenith}}\cos\phi}\right)\right| \tag{6c}$$

Here, ϕ is the latitude angle, ω is the hour angle, and δ is the solar declination, given by [32]:

$$\begin{aligned}\delta &= 0.006918 - 0.399912\cos B + 0.070257\sin B \\ &\quad - 0.006758\cos B + 0.000907\sin 2B \\ &\quad - 0.002697\cos 3B + 0.00148\sin 3B \\ B &= (n-1)\frac{2\pi}{365}\end{aligned} \tag{7}$$

The hour angle, ω, changes with time at the rate of 15 degrees per hour and is zero at solar noon, positive for times after noon, and negative for times before noon. The day of the year is represented by n, which is an integer with values 1–365. Incoming solar rays are not all parallel, due to the apparent size of the sun which converges at the Earth's surface in a solid angle of 9.3 mrad. To approximate the sun shape, a simple distribution model was chosen from Yang et al. [33], according to which radiation is emitted uniformly from the solar disc toward the observer. A uniformly-emitting sphere model was also examined, but did not affect the final results in any significant way.

The magnitude of direct normal solar radiation is modeled using an empirical relationship developed by Meinel and Meinel [34] as cited by [35].

$$I_{\mathrm{D}} = G_0 \tau^{AM^{0.678}} \tag{8}$$

The solar constant G_0 is assumed to be 1367 W/m^2. The atmospheric transmittance, τ, is assumed to be 0.7 for clear-sky conditions. The air mass value AM accounts for the time-dependence of Eq. (8) in the form of the zenith angle. The air mass represents the relative distance of air through which the solar radiation must travel. The simplest relation for air mass at sea level is commonly used as:

$$AM = \frac{1}{\cos\theta_{\mathrm{solar,zenith}}} \tag{9}$$

However, since the simulation location, Albuquerque, is at a high altitude, a relation for the air mass from Kasten and Young [36], which accounts for height above sea level is used:

$$AM = \frac{\exp\left(-0.0001184 h_{\text{altitude}}\right)}{\cos\theta_{\text{solar,zenith}} + 0.5057\left(96.080 - \theta_{\text{solar,zenith}}\right)^{-1.634}} \tag{10}$$

As a consequence of the selected solar model, the direct solar radiation will be symmetric about solar noon for any given day. It should be noted that this particular model does not account for weather effects and assumes clear-sky conditions. However, this does not always imply an optimistic model, as atmospheric conditions can occasionally lead to higher transmissivity than assumed in the model.

3.3. Monte Carlo ray tracing

A Monte Carlo simulation is used to characterize the performance of the field. By using a large set of discrete stochastic energy bundles (rays), the complex, time-dependent interaction between rays and the heliostat field can be characterized statistically. For each simulation, rays are launched from a reference plane above the ground toward the heliostats. If an intersection with a reflector surface occurs, the reflected ray vector is calculated. The ray's path is traced until it intersects with the receiver plane. The position of the intersection relative to the center of the receiver is recorded, allowing the calculation of energy received by different receiver areas over different spans of time.

The general ray-tracing procedure is summarized in the form of a flow chart.

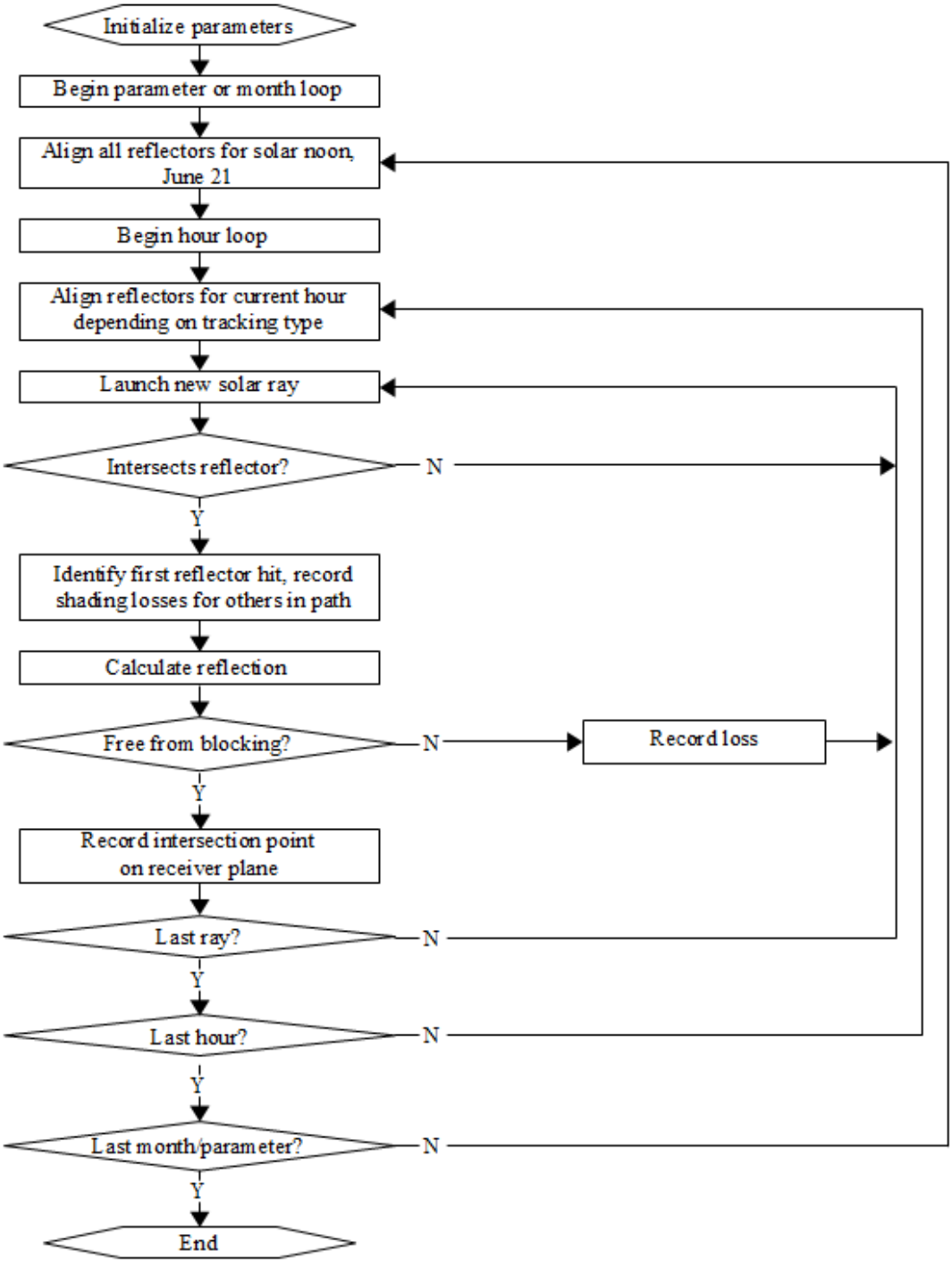

Fig. 7. Flow chart for Monte Carlo ray-tracing simulation.

At the beginning of every simulation, the heliostats are aligned to the receiver. This is done by launching a ray at the center of each reflector, and varying the orientation angles until the reflected ray lands as close to the center of the receiver as possible on the receiver plane. The vector direction of a solar ray reflected by a surface is defined as [37]:

$$\hat{\mathbf{s}}_{\text{reflection}} = \hat{\mathbf{s}}_{\text{solar,center}} - 2\left(\hat{\mathbf{s}}_{\text{solar,center}} \cdot \hat{\mathbf{n}}_{\text{ref},i,j}\right)\hat{\mathbf{n}}_{\text{ref},i,j} \tag{11}$$

where the central solar unit vector is found using Eq. (5). For reflector alignment purposes at solar noon, the reflection is assumed to be perfectly specular with no error and reflected at the center of the reflector surface. After the vector of the reflected ray is determined, the intersection point with the receiver plane is calculated. The receiver plane is tilted about an axis in the y-direction (east-west) as shown in Fig. 2a. The angle of tilt is expressed by θ_{rec}, where $\theta_{\text{rec}} = 0$ is horizontal and $\theta_{\text{rec}} = \pi/2 = 90°$ is vertical. Three points, $\vec{r}_1$, $\vec{r}_2$, and $\vec{r}_3$, can be used to define the plane:

$$\begin{aligned}
\vec{r}_1 &= \vec{r}_{\text{rec,center}} \\
\vec{r}_2 &= \left(r_{\text{rec,center,x}} - \cos\theta_{\text{rec}}\right)\hat{\mathbf{i}} + r_{\text{rec,center,y}}\hat{\mathbf{j}} + \left(r_{\text{rec,center,z}} + \sin\theta_{\text{rec}}\right)\hat{\mathbf{k}} \\
\vec{r}_3 &= r_{\text{rec,center,x}}\hat{\mathbf{i}} + \left(r_{\text{rec,center,y}} + 1\right)\hat{\mathbf{j}} + r_{\text{rec,center,z}}\hat{\mathbf{k}}
\end{aligned} \tag{12}$$

Points $\vec{r}_1$ and $\vec{r}_3$ define the axis of rotation of the receiver plane, while points $\vec{r}_1$ and $\vec{r}_2$ lie along the incline. The plane is then defined mathematically by:

$$Ax + By + Cz + D = 0$$

$$A = \begin{vmatrix} 1 & r_{1,y} & r_{1,z} \\ 1 & r_{2,y} & r_{2,z} \\ 1 & r_{3,y} & r_{3,z} \end{vmatrix} \quad B = \begin{vmatrix} r_{1,x} & 1 & r_{1,z} \\ r_{2,x} & 1 & r_{2,z} \\ r_{3,x} & 1 & r_{3,z} \end{vmatrix} \quad C = \begin{vmatrix} r_{1,x} & r_{1,y} & 1 \\ r_{2,x} & r_{2,y} & 1 \\ r_{3,x} & r_{3,y} & 1 \end{vmatrix} \quad D = -\begin{vmatrix} r_{1,x} & r_{1,y} & r_{1,z} \\ r_{2,x} & r_{2,y} & r_{2,z} \\ r_{3,x} & r_{3,y} & r_{3,z} \end{vmatrix} \tag{13}$$

The point of intersection of the reflected ray with the receiver plane is then found using:

$$\vec{r}_{\text{rec,int}} = \vec{r}_{\text{ref,int}} + u\left(\vec{r}_{\text{reflection}} - \vec{r}_{\text{ref,int}}\right)$$

$$u = \frac{Ar_{\text{ref,int,x}} + Br_{\text{ref,int,y}} + Cr_{\text{ref,int,z}} + D}{A\left(\vec{r}_{\text{ref,int}} - \vec{r}_{\text{reflection}}\right)_{\text{x}} + B\left(\vec{r}_{\text{ref,int}} - \vec{r}_{\text{reflection}}\right)_{\text{y}} + C\left(\vec{r}_{\text{ref,int}} - \vec{r}_{\text{reflection}}\right)_{\text{z}}} \tag{14}$$

The quantity u defines the distance travelled by the reflected ray along its reflection vector before it intersects with the receiver plane. Using the point of reflection at the reflector, the reflection vector, and the distance travelled, the intersection point on the receiver plane is known. Since the unit normal vector of the reflector surface, and therefore the direction of the reflected ray and point of ray intersection with the receiver plane, is a function of $\beta_{i,j}$ and $\varphi_{i,j}$, the distance of the ray–receiver plane intersection point from the center of the receiver can be minimized by varying these angles.

$$f(\beta_{i,j}, \varphi_{i,j}) = \left|\vec{r}_{\text{rec,center}} - \vec{r}_{\text{int,rec}}\right| \tag{15}$$

Therefore the tilt and rotation angles of each reflector are varied such that a function f, given in Eq. (19), is minimized for a ray reflected from the center of the mirror at solar noon on the alignment day. The tracking angle resolution is assumed to be 0.1 degrees in both β and φ, which has been shown to be realizable in low-cost two-axis tracking mechanisms [38]. As the angle increments are constrained to 0.1 degrees, the reflectors are not perfectly aligned, but will be as close to being aligned as possible given the

mechanical range of motion. The reflectors are assumed to have an overall range of motion of $0^\circ < \beta_{i,j} < 60^\circ$ and $-80^\circ < \varphi_{i,j} < 80^\circ$. When the field is aligned according to these criteria, the program begins the transient simulation. In a parametric optimization, this means an hour loop over the specified times for the optimization day of June 21. For an annual simulation, the code runs through those specified hours for one day on each month of the year. In both cases, an hour loop performs field alignment and ray tracing operations for each hour on the relevant day.

The simulation proceeds through the flow chart process illustrated in Fig. 7. Each ray is launched with a prescribed power based on the calculated direct irradiance level, the launch area, the projection of the incident radiation onto the horizontal ground, and the number of rays used:

$$\dot{Q}_{\text{ray}} = \frac{I_{\text{D}} A_{\text{launch}} \left(-\hat{\mathbf{n}}_{\text{ground}} \cdot \hat{\mathbf{s}}_{\text{solar,center}}\right)}{N_{\text{rays}}} \qquad (16)$$
$$\hat{\mathbf{n}}_{\text{ground}} = 0\hat{\mathbf{i}} + 0\hat{\mathbf{j}} + 1\hat{\mathbf{k}}$$

Rays are launched with uniform distribution of azimuth angles $\gamma_{\text{solar,deviation}}$ from 0–2π and polar angles $\theta_{\text{solar,deviation}}$ as specified in Eq. (8a).

$$\theta_{\text{solar,deviation}} = \arctan\left(\sqrt{\Re_\theta}\,\tan\left(\theta_{\text{solar,max}}\right)\right) \qquad (17a)$$

$$\gamma_{\text{solar,deviation}} = 2\pi\Re_\gamma \qquad (17b)$$

Here, $\Re_\theta$ and $\Re_\gamma$ are random numbers from 0–1 and $\theta_{\text{solar,max}}$ is the solar half-cone angle, or 4.65 mrad. The solar vector accounting for the sunshape approximation is then:

$$\hat{\mathbf{s}}_{\text{solar}} = \sin\theta_{\text{solar,deviation}}\left[\cos\gamma_{\text{solar,deviation}}\hat{\mathbf{t}}_1 + \sin\gamma_{\text{solar,deviation}}\hat{\mathbf{t}}_2\right] + \cos\theta_{\text{solar,deviation}}\hat{\mathbf{s}}_{\text{solar,center}} \tag{18}$$

Variables $\hat{\mathbf{t}}_1$ and $\hat{\mathbf{t}}_2$ represent unit vectors in a plane perpendicular to the direction of the unmodified solar ray. To calculate them, first the vector is found which is perpendicular to the unmodified solar ray at its base and intersects a vertical reference line, taken to be the line (0,0,*z*). The intersection point is found as:

$$\vec{r}_{\text{launch,tangent,int}} = 0\hat{\mathbf{i}} + 0\hat{\mathbf{j}} + \left[\frac{\left(-\mathbf{s}_{\text{solar},x}\left(0 - r_{\text{launch},x}\right) - \mathbf{s}_{\text{solar},y}\left(0 - r_{\text{launch},y}\right)\right)}{\mathbf{s}_{\text{solar},z}} + r_{\text{launch},z}\right]\hat{\mathbf{k}} \tag{19}$$

Then $\hat{\mathbf{t}}_1$ and $\hat{\mathbf{t}}_2$ are found as:

$$\hat{\mathbf{t}}_1 = \frac{\vec{r}_{\text{launch,tangent,int}} - \vec{r}_{\text{launch}}}{\left|\vec{r}_{\text{launch,tangent,int}} - \vec{r}_{\text{launch}}\right|} \tag{20a}$$

$$\hat{\mathbf{t}}_2 = \hat{\mathbf{s}}_{\text{solar}} \times \hat{\mathbf{t}}_1 \tag{20b}$$

For all simulations, rays are launched from within a specified launch area with a uniform distribution of starting locations. In order to provide coverage of the whole field, the launch area is taken to extend 25% beyond the edge of the field in each direction. The bounds of the launch area centered about the reflector field are then:

$$x_{\text{launch,min}} = 0 - 0.25\left(\left(N_{\text{rows}} - 1\right)d_{\text{spacing}}\right) \tag{21a}$$

$$x_{\text{launch,max}} = \left(N_{\text{rows}} - 1\right)d_{\text{spacing}} + 0.25\left(\left(N_{\text{rows}} - 1\right)d_{\text{spacing}}\right) \tag{21b}$$

$$y_{\text{launch,min}} = 0 - 0.25\left(\left(N_{\text{cols}} - 1\right)d_{\text{spacing}}\right) \tag{21c}$$

$$y_{\text{launch,max}} = \left(N_{\text{cols}} - 1\right)d_{\text{spacing}} + 0.25\left(\left(N_{\text{cols}} - 1\right)d_{\text{spacing}}\right) \tag{21d}$$

The launch area is then:

$$A_{\text{launch}} = \left(x_{\text{launch,max}} - x_{\text{launch,min}}\right)\left(y_{\text{launch,max}} - y_{\text{launch,min}}\right) \tag{22}$$

For each ray, every reflector surface is checked for intersection. Checking begins on the corner of the field closest to the sun's current position. In the northern hemisphere, this means the south-east corner in the morning and the south-west corner in the afternoon. In this way, the first calculated intersection is the true reflector struck, and any further heliostats in the ray's path are shaded by the first. The reflector surfaces have a surface curvature defined by a sphere; therefore, the intersection is calculated first for the line-sphere. A second check must be performed to ensure that the intersection is within the square aperture area. This is done by first finding the point along the reflector's normal vector that, when connected to the calculated intersection point on the sphere, will form a vector perpendicular to the reflector center's normal vector.

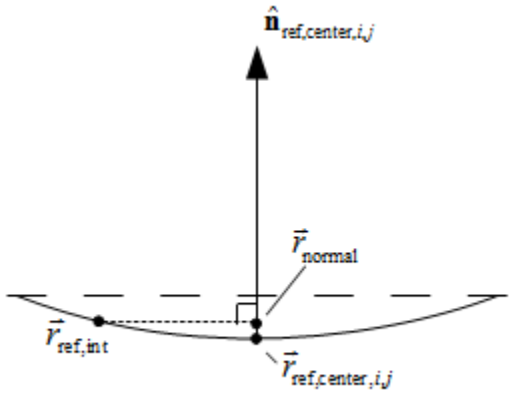

Fig. 8. Side-view illustration showing construction of vectors to check for intersection with the reflector aperture area.

Finally, the distance components from the intersection point to the calculated point along the reflector center's normal vector in a plane parallel to the aperture are checked to make sure that the point does represent a true intersection with the reflector surface.

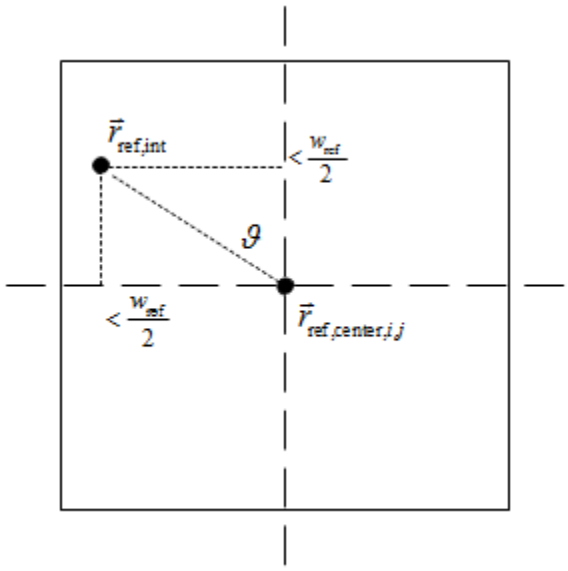

Fig. 9. View of square aperture projection. Perspective is in the anti-normal direction of the reflector center.

$$\left|\vec{r}_{\text{normal}} - \vec{r}_{\text{ref,int}}\right| \cos\vartheta < \frac{w_{\text{ref}}}{2}$$
$$\text{and} \tag{23}$$
$$\left|\vec{r}_{\text{normal}} - \vec{r}_{\text{ref,int}}\right| \sin\vartheta < \frac{w_{\text{ref}}}{2}$$

If the intersection is found to be a true intersection with the reflector surface, the ideal reflection vector is calculated from Eq. (11) based on the normal vector on the surface at the point of intersection.

It is assumed that there is some level of optical error present in the concentrating system, which may be a combination of surface slope, tracking, and other errors. For this work it is assumed that the general optical error can be characterized by the RMS value of the surface slope error and tracking errors for the motion in β and φ. This error is accounted for in the numerical analysis by modifying the normal vector by which the reflection vector is calculated. Assuming a constant optical error σ_{optical}, the polar and azimuthal angles of deviation from the ideal reflection vector are found:

$$\sigma_{\text{optical}} = \sqrt{\left(\sigma_{\text{slope}}\right)^2 + \left(\sigma_{\beta}\right)^2 + \left(\sigma_{\varphi}\right)^2} \tag{24a}$$

$$\Re_{\theta} = \frac{1 - \text{erfc}\left(\dfrac{\theta_{\text{ray,deviation}}}{\sqrt{2}\sigma_{\text{optical}}}\right)}{1 - \text{erfc}\left(\dfrac{\pi}{2\sqrt{2}\sigma_{\text{optical}}}\right)} \tag{24b}$$

$$\Re_{\gamma} = \frac{2\pi}{\gamma_{\text{ray,deviation}}} \tag{24c}$$

$$\hat{\mathbf{n}}^{*}_{\text{ref},i,j} = \sin\theta_{\text{ray,deviation}}\left[\cos\gamma_{\text{ray,deviation}}\hat{\mathbf{t}}_1 + \sin\gamma_{\text{ray,deviation}}\hat{\mathbf{t}}_2\right] + \cos\theta_{\text{ray,deviation}}\hat{\mathbf{n}}_{\text{ref},i,j} \tag{24d}$$

When combined with a randomly-generated azimuth angle from 0 to 2π, this expression generates a set of polar deviation angles with an average of 0 and a standard deviation of σ_{optical}. The method was statistically verified by recording deviation angles throughout the simulations and calculating the mean and standard deviation of the polar deviation angles.

The reflected ray is then checked for blocking, which is the result of intersection with the backs of other reflector surfaces on the reflected ray's path to the receiver plane. Finally, if no blocking is encountered, the intersection with the receiver plane is calculated and the ray's energy over the hour multiplied by the reflectivity of the mirror is added to a running sum of receiver energy for the current hour. Sums of energy at the receiver plane are recorded for receiver sizes of radius 0.05–0.50 m about the receiver center in increments of 0.05 m for quick reference, and the intersection positions of all individual rays are recorded for more advanced processing such as the generation of heat flux maps. A nominal receiver radius of 0.35 m, corresponding to the approximate size of 200 kW-range volumetric receivers reported in the literature [11], is assumed for all cases except when stated otherwise.

A number of losses occur in the optical system which must be accounted for, including cosine loss, shading, surface reflectivity, blocking, and spillage. The cosine loss represents a loss due to off-normal alignment of the reflector surface with the incident solar ray, which allows less radiation to be reflected. Depending on the heliostat configuration and the direction of solar radiation, shading can occur when multiple heliostats are in the incident ray's path. At the point of reflection there will be some energy loss due to the reflectivity of the surface. After reflection, the ray may strike the back of another heliostat on its way to the receiver. Finally, the reflected ray may not land within the receiver area, introducing a spillage effect. These factors can be combined into an overall optical efficiency for a given time period Δt:

$$\eta_{\text{optical}} = \eta_{\text{cosine}}\eta_{\text{shading}}\eta_{\text{reflection}}\eta_{\text{blocking}}\eta_{\text{spillage}} = \frac{\int_{\Delta t}\dot{Q}_{\text{rec}}\,\mathrm{d}t}{\int_{\Delta t}\dot{Q}_{\text{ref,max}}\,\mathrm{d}t} \tag{25}$$

This efficiency represents the energy reflected to the specific receiver area divided by the maximum possible energy that can be intercepted by the total reflector area. The representative instantaneous concentration ratio for a given hour and the time-average concentration ratio over a time period Δt are calculated as:

$$C = \frac{q''_{\text{rec}}}{\left(1\ \frac{\text{kW}}{\text{m}^2}\right)\left(\pi {R_{\text{rec}}}^2\right)} \tag{26a}$$

$$\bar{C} = \frac{\int_{\Delta t}\dot{Q}_{\text{rec}}\,\mathrm{d}t}{\left(1\ \frac{\text{kW}}{\text{m}^2}\right)\left(\pi {R_{\text{rec}}}^2\right)\Delta t} \tag{26b}$$

The longest time over which averaging occurs is one day, which is assumed to be a quantity of hours about solar noon. For annual simulations, the field is simulated on a representative day for each month, as suggested by Duffie [31]. The average days are listed for each month in Table 3.

Table 3. Representative day for each month used in annual simulation.

Month	Number of days	Representative day of month	Representative day of year
January	31	17	17
February	28	16	47
March	31	16	75
April	30	15	105
May	31	15	135
June	30	11	162
July	31	17	198
August	31	16	228
September	30	15	258
October	31	15	288
November	30	14	318
December	31	10	344

Chapter 4. Optical concentrator evaluation

The design point parameters of the optical concentrator field are selected by an iterative optimization process. The parameters varied for analysis of the optical field include: reflector curvature, the number of different reflector curvatures used throughout the field, reflector width, reflector spacing, receiver vertical position, and optical error.

4.1. Reflector curvature

The reflector surfaces are given a slight spherical curvature to assist in concentration. Maintaining a square aperture area, an individual reflector surface is shaped as in Fig. 10.

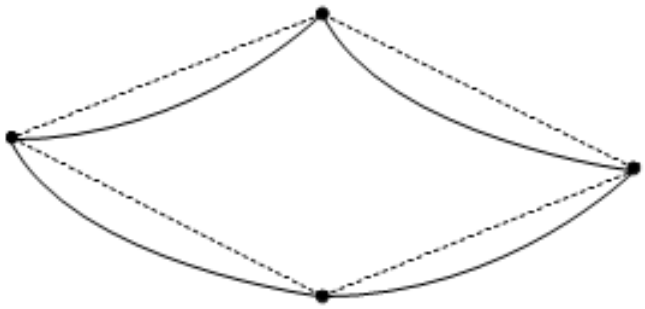

Fig. 10. Diagram demonstrating spherical curvature (exaggerated for effect) and square aperture projection.

The ratio of surface curvature, defined as the sphere radius, to the focal length is varied to determine the optimum value. A numerical simulation was implemented to test the spread of rays striking the receiver plane as a function of the ratio of the curvature radius to the

focal length. Both a close and far reflector were tested. The distance from the receiver center was recorded for each ray reflected to the receiver plane, and the standard deviation of the distances calculated. The plot in Fig. 11 shows the results for three cases: a far reflector with 2.5 mrad optical error, a far reflector with 0.0 mrad optical error, and a close reflector with 0.0 mrad optical error.

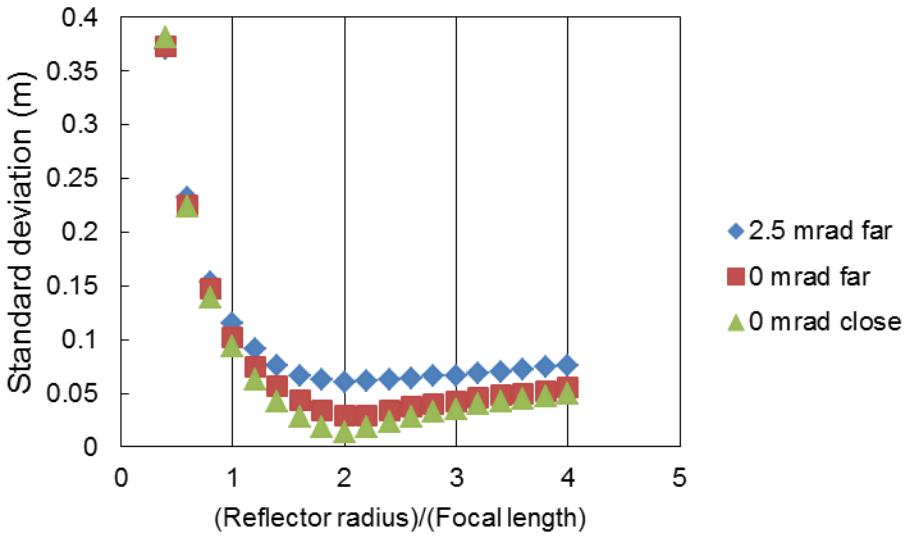

Fig. 11. Standard deviation of distance of ray termination point from receiver center vs. the ratio of reflector curvature radius to focal length.

The reflector radius of curvature should be twice the intended focal length, which is confirmed in the literature [39]. The actual ray paths were recorded and read into a VPython script to visualize the effect in 3-D space.

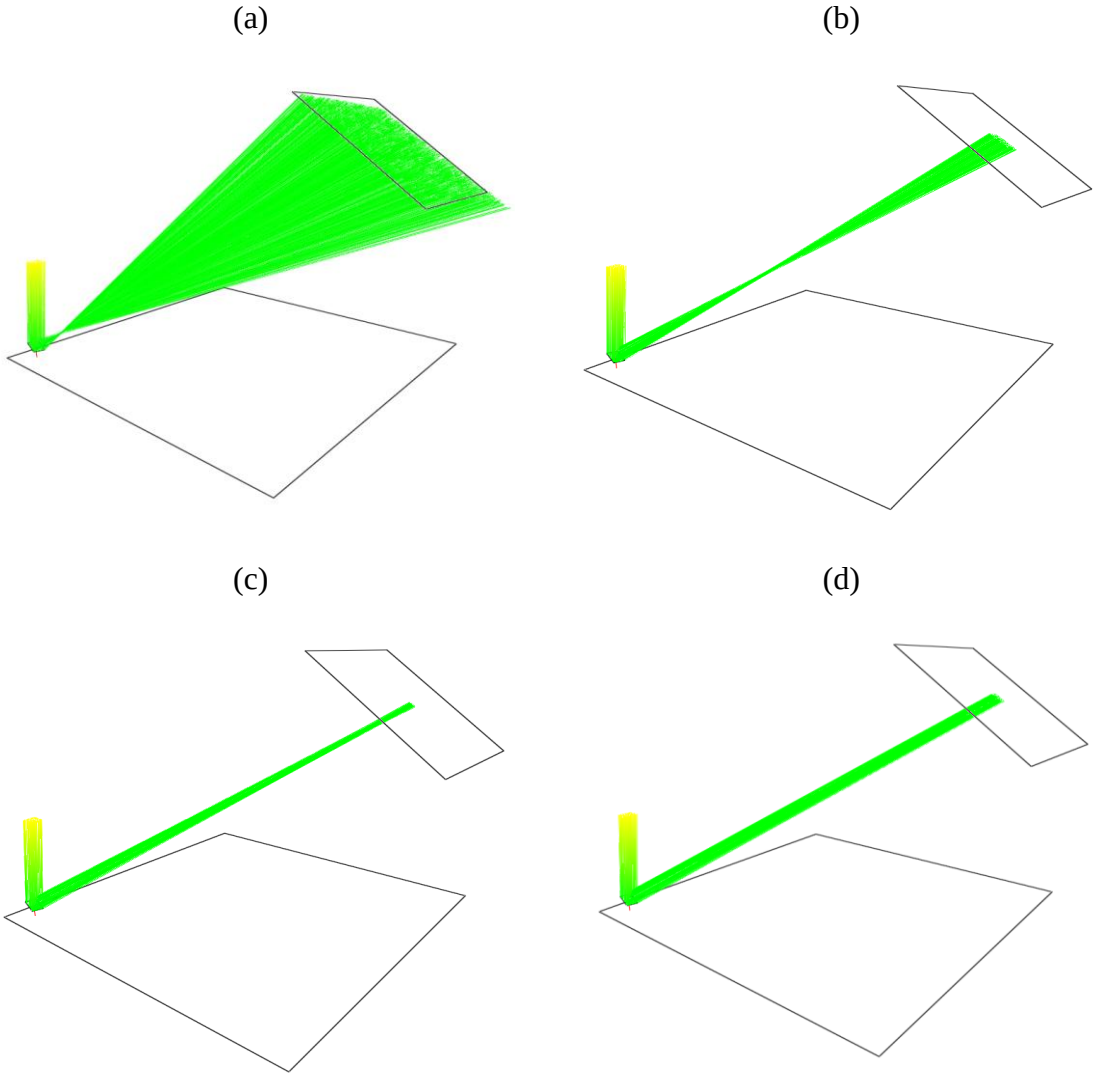

Fig. 12. Ray traces for a single reflector with reflector curvature radius to focal length ratio of (a) 0.2, (b) 1.0, (c) 2.0, (d) 4.0.

The ray traces in Fig. 12 provide a good visualization of the impact of a reflector radius that is either larger or smaller than ideal. If the reflector radius is too small, the rays will focus in between the reflector and the receiver and spread before they can reach the target. If the radius is too large, the focal point to be beyond the target. However, since

the rays do not focus before the target and spread in this case, the image error may not be as dramatic when the reflector radius is larger-than-ideal. In the case of non-ideal radius matching, these results indicate that too large a reflector radius is preferable to a radius that is too small.

4.2. Number of reflector radii

While each reflector surface would ideally be curved according to its specific location in the field, it is more practical from a design, manufacturing, and maintenance standpoint to limit the number to a few curvatures. When limiting the number of different curvatures, a number of "bins" is set up equal to the number of desired radii in order to distribute different values of radii appropriately throughout the field. The outer boundaries of the entire bin domain are the distance from the receiver center to the closest and the farthest reflector, whose position is calculated according to the top of its stationary post (point B in Fig. 5). The difference in maximum and minimum distance is divided evenly such that the number of bins equals the number of desired radii in the field. An illustration of this concept with simple example numbers is provided in Fig. 13.

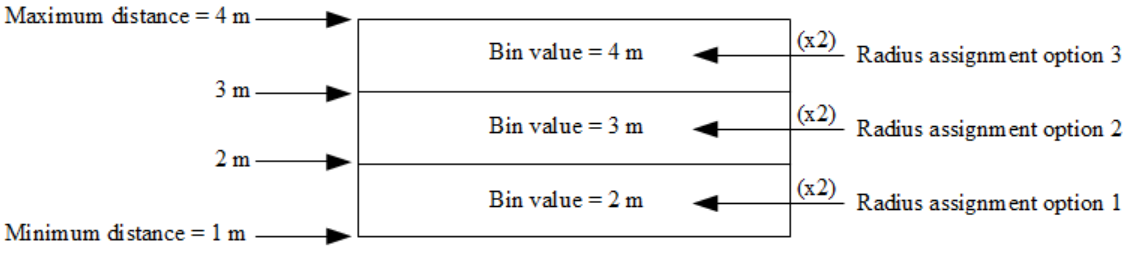

Fig. 13. Illustration of radius "bin" concept.

In this example the radius options for the reflectors would be twice each of the maximum bin values, or 4 m, 6 m, and 8 m. The program then sweeps through the field, calculating the distance from the top of the stationary post to the receiver center for each reflector. Each reflector receives a curvature radius assignment equal to twice the maximum bin value corresponding to the bin in which its actual distance falls. In this way, the number of desired radii can be varied and the appropriate values assigned dynamically throughout the field. Using this algorithm, imperfect assignments will always cause larger-than-ideal curvature radii, which leads to less dramatic image spreading as described in the preceding section

The effect of the number of unique radii is analyzed. Since increasing the number of radii effectively just reduces the image error, it is expected that the optical performance will be worst when using 1 reflector radius and will improve as more are used. At some point, performance gains become negligible and it is no longer beneficial to add complexity to the system by way of additional components. Since the relations used for the solar position and direct radiation are symmetric about solar noon and in the interest of efficient computation time, only the hours -4, -2, and 0 (8am, 10am, and noon) are simulated. Lines are used to connect the points on the plots for each parameter value for readability, but do not necessarily suggest a means for interpolation.

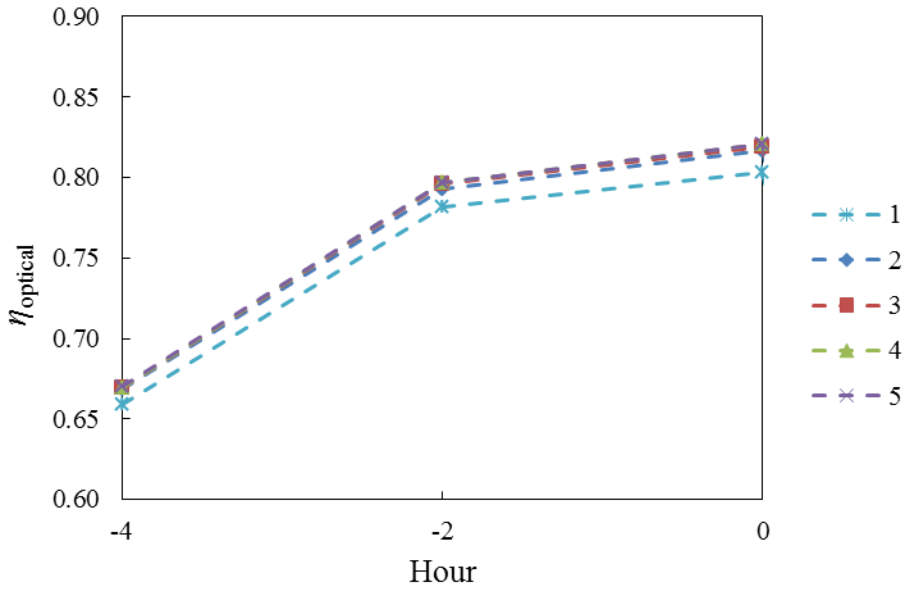

Fig. 14. Optical efficiency at select hours of the optimization day for different numbers of reflector radii used in the field. Connecting lines used for readability and do not suggest a means for interpolation.

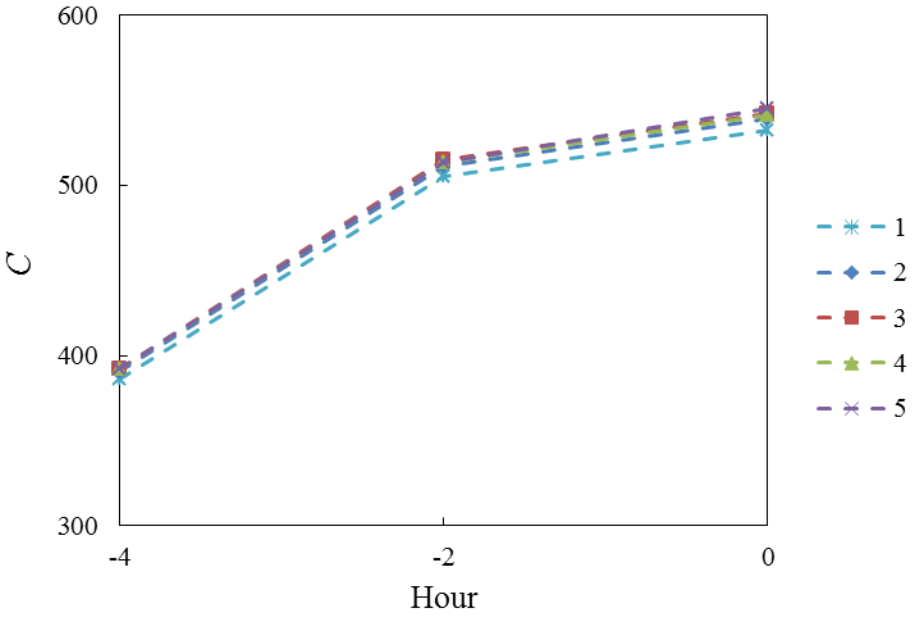

Fig. 15. Concentration ratio at select hours of the optimization day for different numbers of reflector radii used in the field.

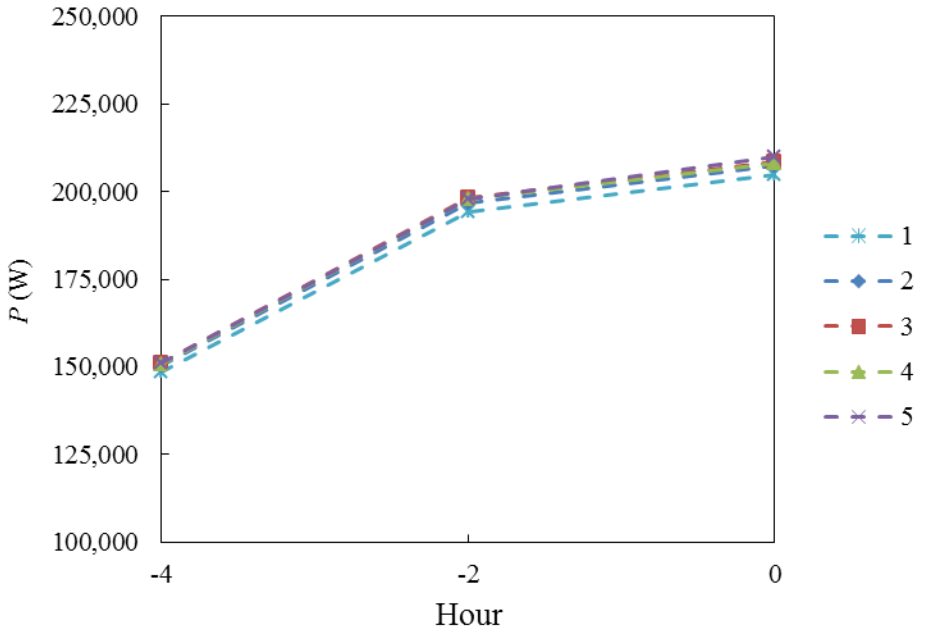

Fig. 16. Thermal power striking receiver at select hours of the optimization day for different numbers of reflector radii used in the field.

The simulation results show that gains from adding additional reflector radii beyond three are negligible. The design point condition of three unique reflector radii is therefore chosen for the subsequent annual simulation.

4.3. Reflector width

The size of the reflectors is considered in terms of aperture area side length. A range of side lengths from 0.5–1.0 m (0.25–1.0 m^2 aperture area) is considered. Smaller sizes will reflect less energy but will be more efficient for the same receiver size because of decreased spillage. Larger sizes will reflect more energy but more energy will also miss the receiver because of increased image size for imperfect reflections, decreasing the

efficiency. Currently the smallest reflector surfaces in large production are the 1.14 m^2 reflectors used by eSolar [22]. However, these are still used for relatively large outputs, on the order of 5 MWe for the Sierra SunTower. In contrast to the popular trend of increasing heliostat size [22,23], small reflectors can decrease production costs by allowing manufacturing to be done in factories instead of onsite [22]. Small reflectors are also easier to manufacture with very high accuracy [23] and can reduce the effects of wind loading due to attenuation throughout the field [22].

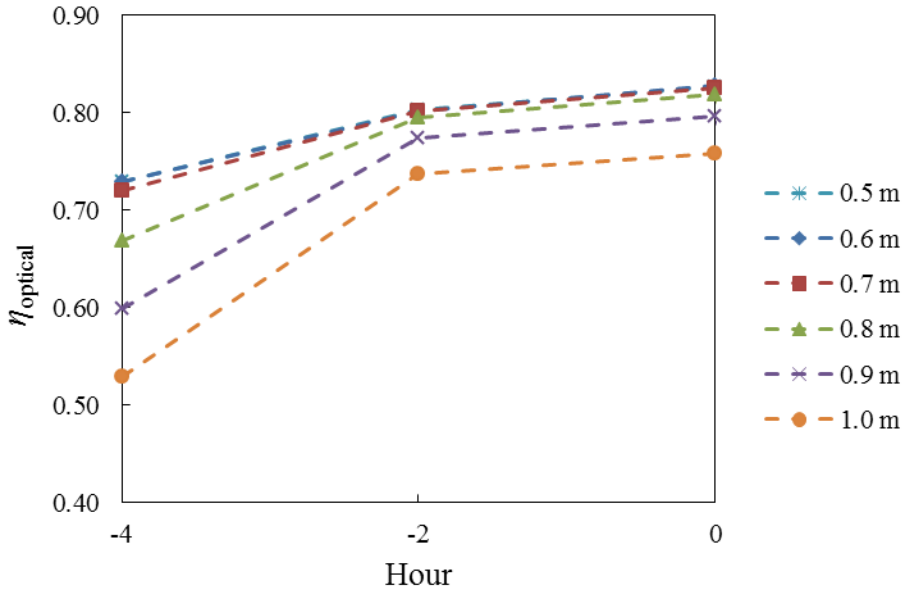

Fig. 17. Optical efficiency at select hours of the optimization day for different reflector side lengths.

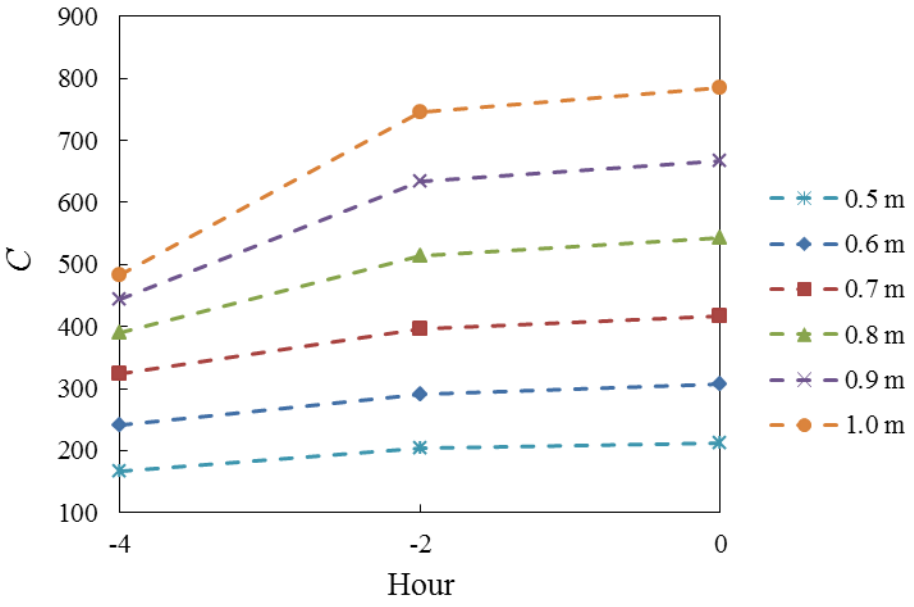

Fig. 18. Concentration ratio at select hours of the optimization day for different reflector side lengths.

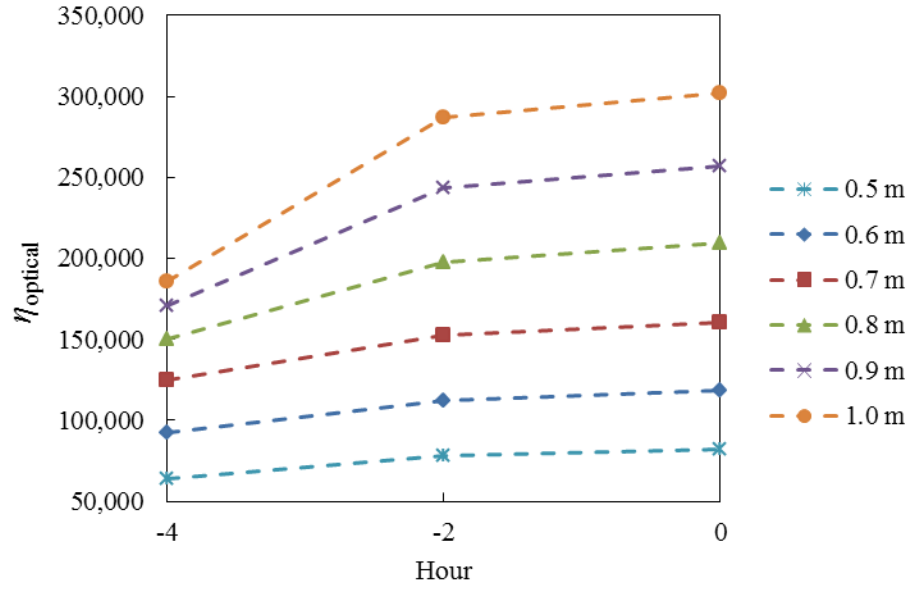

Fig. 19. Thermal power striking the receiver at select hours of the optimization day for different reflector side lengths.

The choice of side lengths of the reflectors is a trade-off between efficiency and concentration ratio or thermal power delivery. A side length of 0.8 m is selected for the present design point condition as it allows delivery of slightly higher than 200 kW at solar noon, corresponding to similarly-size volumetric gas receivers, while also reaching a peak optical efficiency above 80%.

4.4. Reflector spacing

The distance reflectors are separated is an important factor in ensuring that minimal blocking occurs while still efficiently utilizing ground space. In addition, placing them too far apart can amplify the effects of optical error because of the increased radiation path length. The spacing from post-to-post is varied between 110–150% of the width of a single reflector.

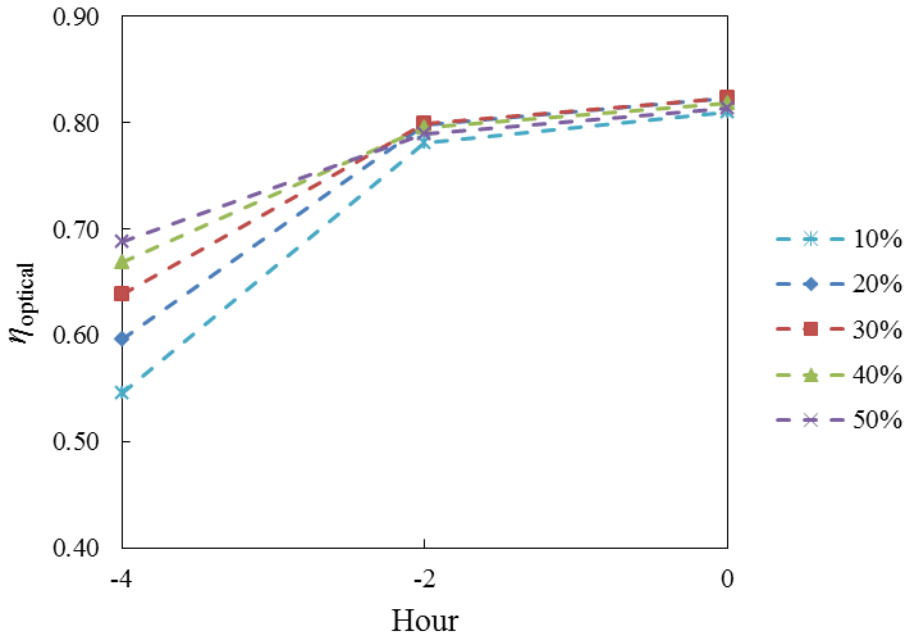

Fig. 20. Optical efficiency at select hours of the optimization day for different reflector spacings.

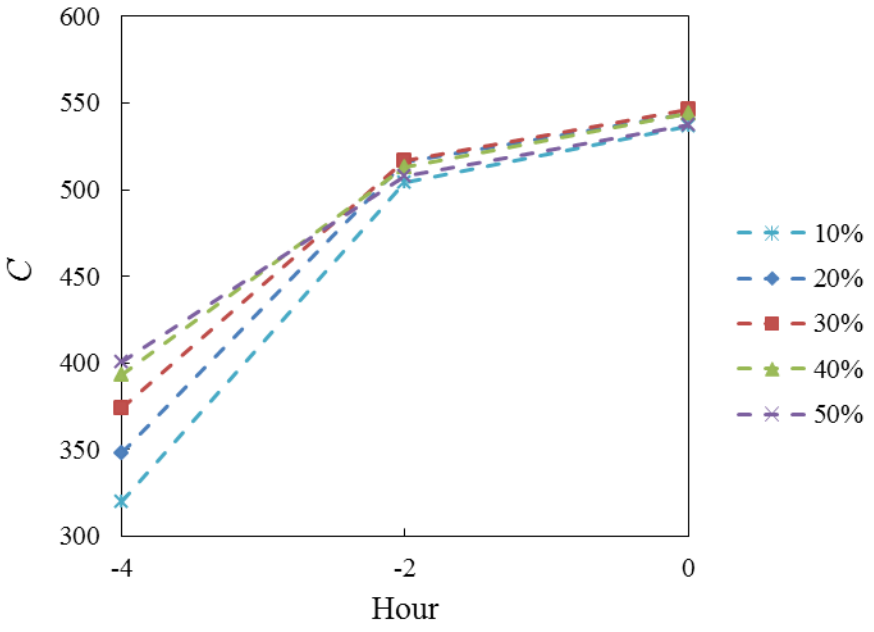

Fig. 21. Concentration ratio at select hours of the optimization day for different reflector spacings.

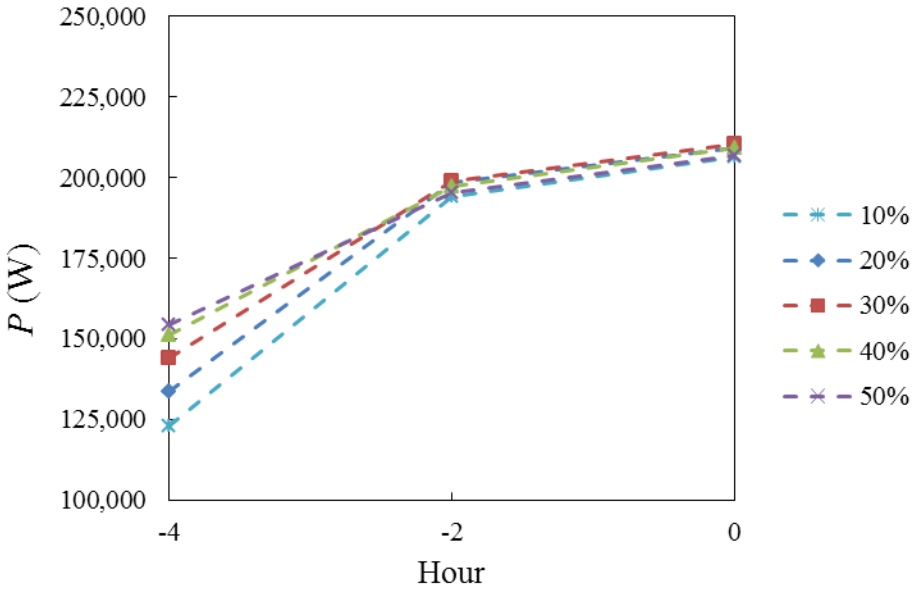

Fig. 22. Thermal power striking the receiver at select hours of the optimization day for different reflector spacings.

A spacing of 40% (140% the side length of one reflector between each heliostat post) is selected as a result of the optimization. This value offers very high performance at solar noon with above-average performance compared to the other values at off-noon times. Heliostat field designs are often partially characterized by their ground factor, or the ratio of total reflector aperture area to total ground footprint. For the design point parameters, this leads to a ground factor value of:

$$F_g = \frac{N_{ref} A_{ref}}{\left[\left(N_{ref,i} - 1\right)\left(d_{spacing}\right) + 2w_{ref}\right]^2} = \frac{400 \times 0.64 \text{ m}^2}{\left[\left(20-1\right)\left(1.4 \times 0.8 \text{ m}\right) + 0.8 \text{ m}\right]^2} = 0.525 \quad (27)$$

A ground factor value of 52.5% is very high compared to typical, larger-scale heliostat configurations, which are often lower than 30% [19]. This suggests that the current

configuration makes efficient use of ground space and may contribute to its appeal for use in distributed or urban settings where size may be of concern.

4.5. Receiver position

The vertical position of the receiver is varied in the simulation from 10–20 m above the field. By raising the position of the receiver, rays are reflected at a steeper trajectory. This allows for reduced blocking, as rays are less likely to hit the low heliostats in front of them. However, at some point this gain is mitigated by the increasing image size due to imperfect reflection and focusing.

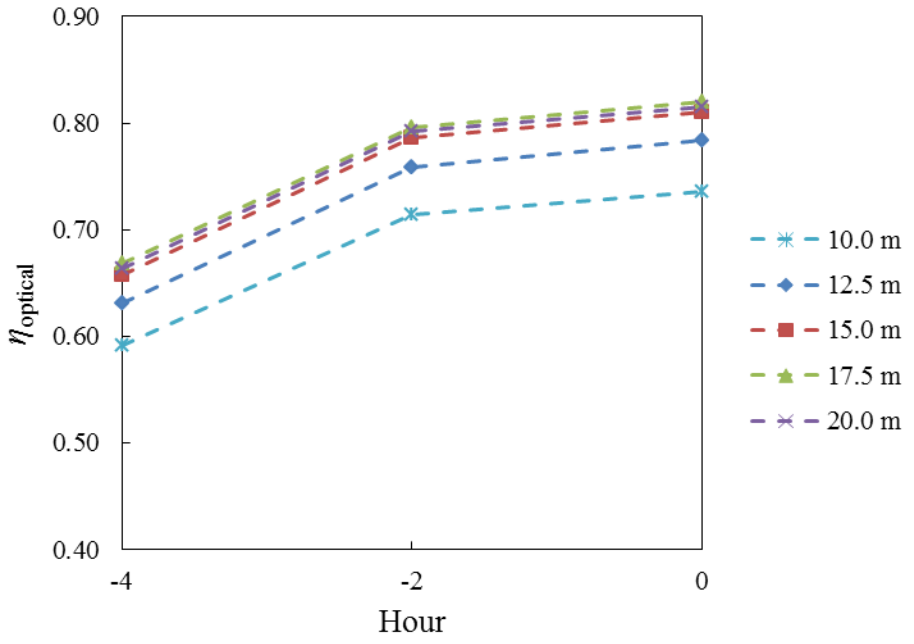

Fig. 23. Optical efficiency at select hours of the optimization day for different vertical positions of the receiver center.

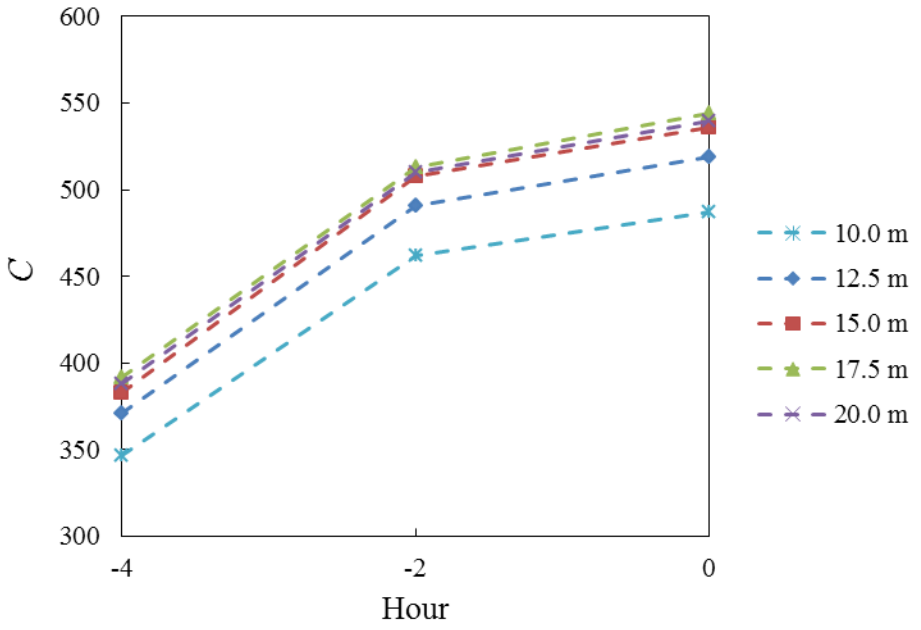

Fig. 24. Concentration ratio at select hours of the optimization day for different vertical positions of the receiver center.

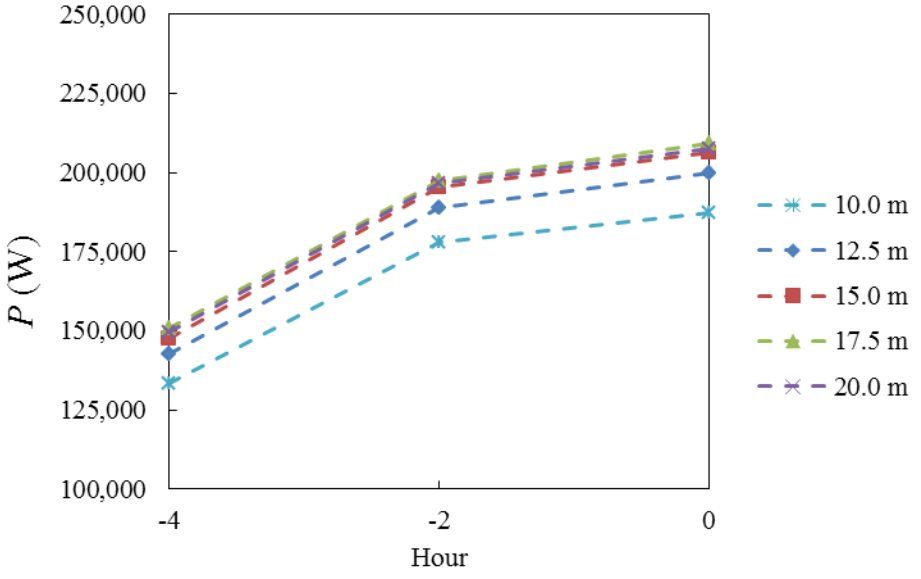

Fig. 25. Thermal power striking the receiver at select hours of the optimization day for different vertical positions of the receiver center.

Performance increases up to a receiver position of 17.5 m above the ground because of the reduction in blocking losses, then is reduced slightly for a position of 20.0 m due to increased image size. The 17.5 m position is selected as the design point condition.

4.6. Optical error

As a final consideration, the overall optical error derived from Eq. (22) is varied. The design point optical error is assumed to be due to a 2.0 mrad slope error and 1.7 mrad (0.1 degrees) tracking errors in both angles. From Eq. (22) this gives 3.13 mrad. A value of 3.5 mrad is conservatively used. It should be noted that variation of this parameter does not allow for optimization of the system in the same sense as the other parameters. Rather, it provides a reference for the effects of differing optical error on overall performance. This can become important when selecting reflector materials and for predicting the change in system performance over time as the reflector surfaces become dirty or damaged.

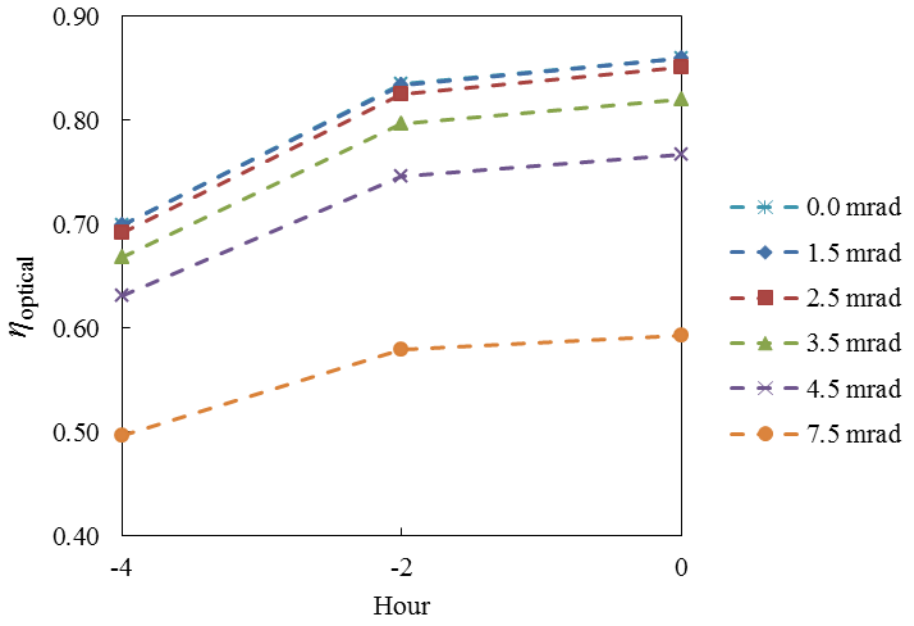

Fig. 26. Optical efficiency at select hours of the optimization day for different values of overall optical error.

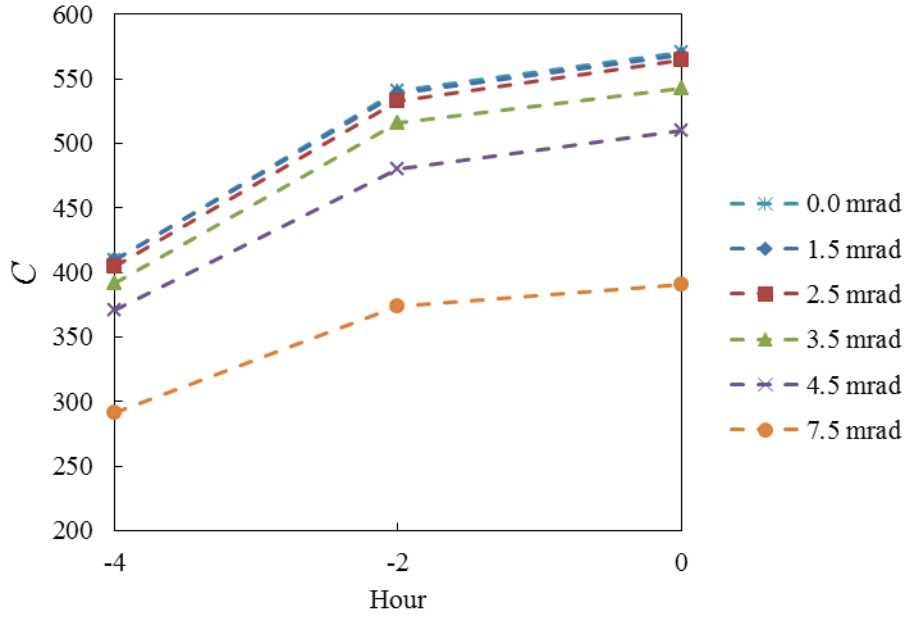

Fig. 27. Concentration ratio at select hours of the optimization day for different values of overall optical error.

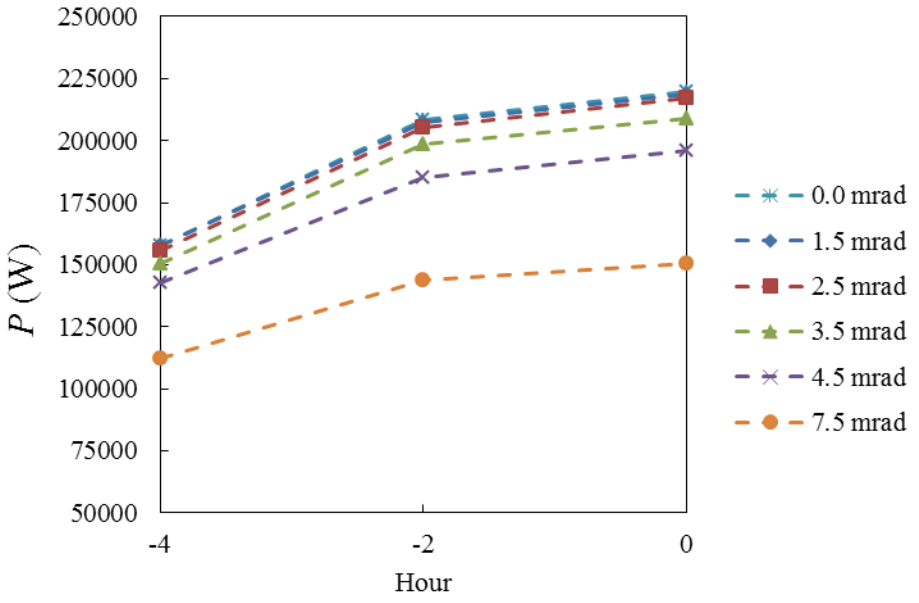

Fig. 28. Thermal power striking the receiver at select hours of the optimization day for different values of overall optical error.

The results show that considerable performance gains can be achieved if the overall optical error could be reduced from 3.5 mrad to 2.5 mrad. It is also worth noting that the case of an overall optical error of 1.5 mrad performs nearly identically to the case of perfectly-specular mirrors. Conversely, surfaces with an optical error of 7.5 mrad suffer significant penalties. At solar noon the optical efficiency plummets from a design point performance of 82.0% to 59.3%.

4.7. Iteration process

The optimization procedure progressed through four iterations to arrive at the design point. Each iteration varied all six parameters through a range determined by the results

of the previous iteration. Since each parametric optimization included a simulation at the iteration's design point, an average field efficiency and concentration ratio was calculated from 6 result sets.

Table 4. Progression of optimization iterations, including nominal, minimum, and maximum values for each parameter.

Parameter	Iteration 1 nominal value	Range	Iteration 2 nominal value	Range	Iteration 3 nominal value	Range	Iteration 4 nominal value	Range
N_{radii}	1	1–5	2	1–5	2	1–5	3	1–5
$r_{rec,z}$ (m)	5	5–15	15	10–20	15	10–20	17.5	10–20
2 x w_{ref} (m)	0.5	0.5–1.0	0.7 m	0.5–1.0	0.8 m	0.5–1.0	0.8 m	0.5–1.0
$d_{spacing}$	20%	10–50%	30%	10–50%	30%	10–50%	40%	10–50%
$\sigma_{optical}$ (mrad)	3.5	0–7.5	3.5	0–7.5	3.5	0–7.5	3.5	0–7.5
$\eta_{optical,noon}$	0.641		0.838		0.809		0.819	
C_{noon}	165.6		424.7		536.0		542.7	
P_{noon} (W)	63,743.0		163,438.8		206,264.3		208,846.4	

The nominal design point parameters chosen for iteration 4 were found to give the best performance, and were selected as the nominal parameter values for the annual simulation.

4.8. Annual system performance

For the annual system performance, the optimized parameters for the optical concentrator found through the described parametric analysis are used. Additionally, potential cost savings are explored by simulating five different linked tracking configurations as well as the nominal case of full individual tracking. A decrease in performance is expected by linking heliostats together, but a decrease in cost and complexity is possible as each linkage group can share a common drive. The tracking types and their labels are

described in Table 5.

Table 5. Summary of heliostat linkage configurations.

Tracking type label	Number of linked heliostats	Description of linkage
TT-1x1	1	All heliostats are tracking individually
TT-1x2	2	Linkages of 1 (east-west) x 2 (north-south) heliostat groups
TT-2x1	2	Linkages of 2 (east-west) x 1 (north-south) heliostat groups
TT-2x2	4	Linkages of 2x2 heliostat groups
TT-4x4	16	Linkages of 4x4 heliostat groups
TT-5x5	25	Linkages of 5x5 heliostat groups

The alignment procedure for the linked tracking configurations follows the same general principle as the individual tracking mode. However, the groups are aligned by minimizing the sum of their reflected rays' distances to the receiver center. Annual optical simulations are carried out for 6 tracking setups, 9 hours per day (for a day selected as representative of the month), and 12 months per year for a total of 648 ray tracing procedures requiring 648 million rays. Before a suitable performance comparison between the tracking types can be made using the annual data, it is necessary to fix the size of the receiver area on the aperture plane. For a 5, 7, and 9 hour operation time, Fig. 29Fig. 31 present optical efficiency and concentration ratio curves for each tracking type as a function of receiver radius R_{rec}.

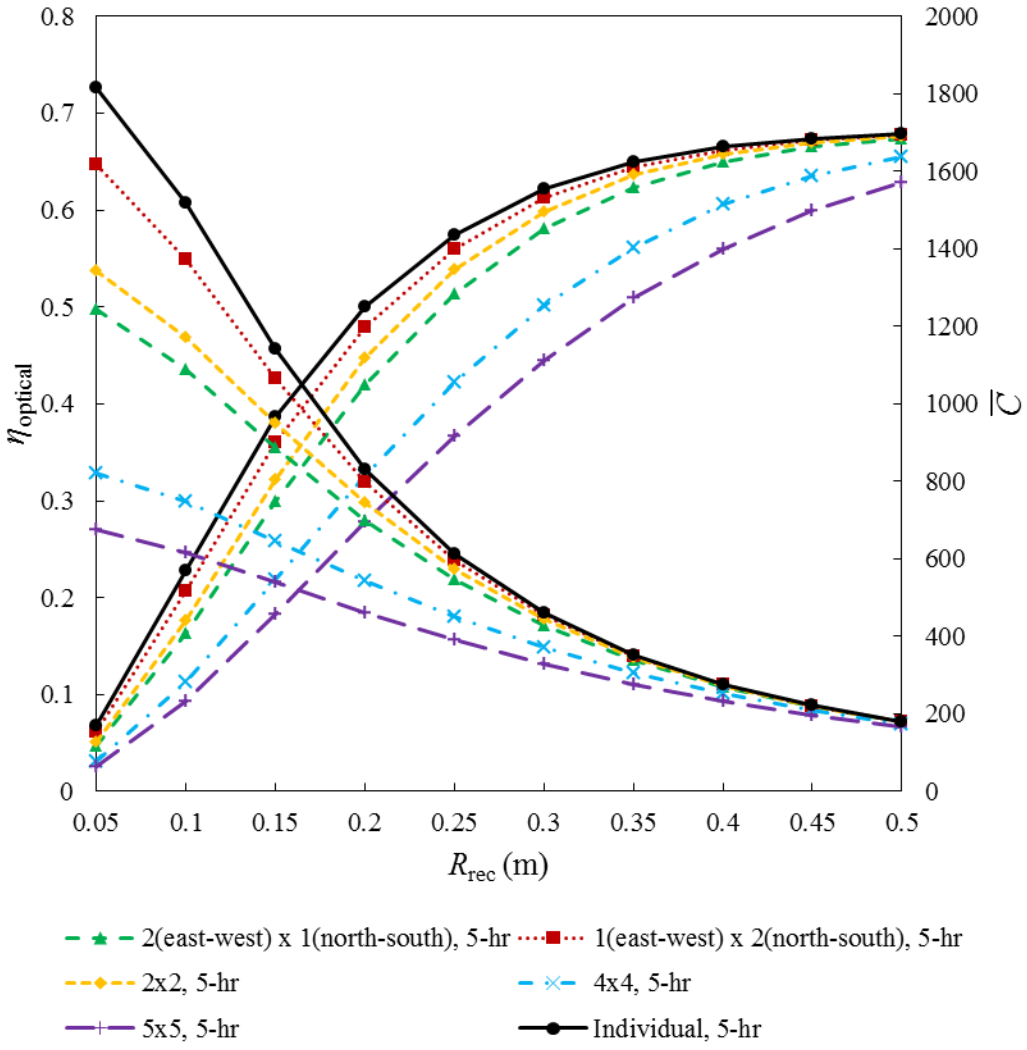

Fig. 29. Optical efficiency (left axis) and concentration ratio (right axis) for different receiver sizes and 5 hours of operation about solar noon in the month of December.

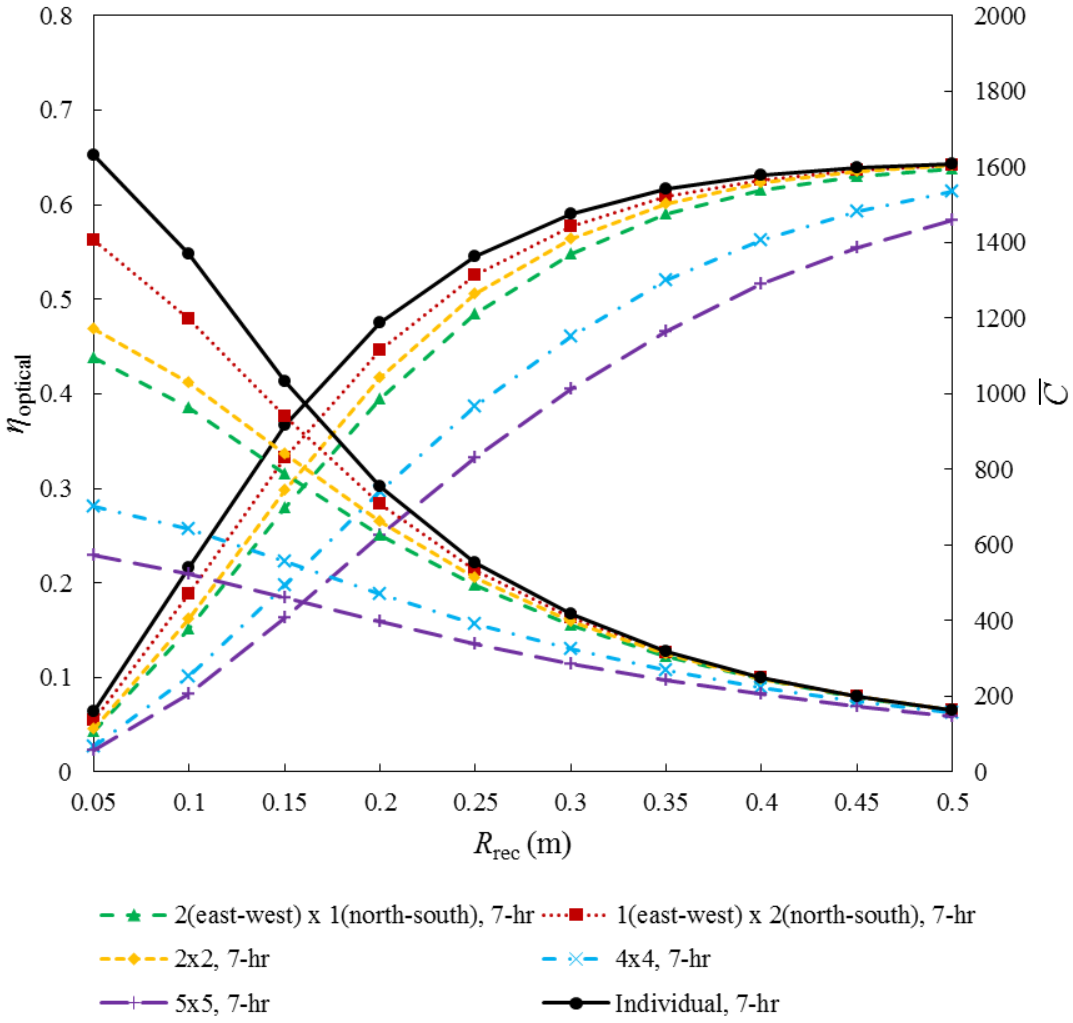

Fig. 30. Optical efficiency (left axis) and concentration ratio (right axis) for different receiver sizes and 7 hours of operation about solar noon in the month of December.

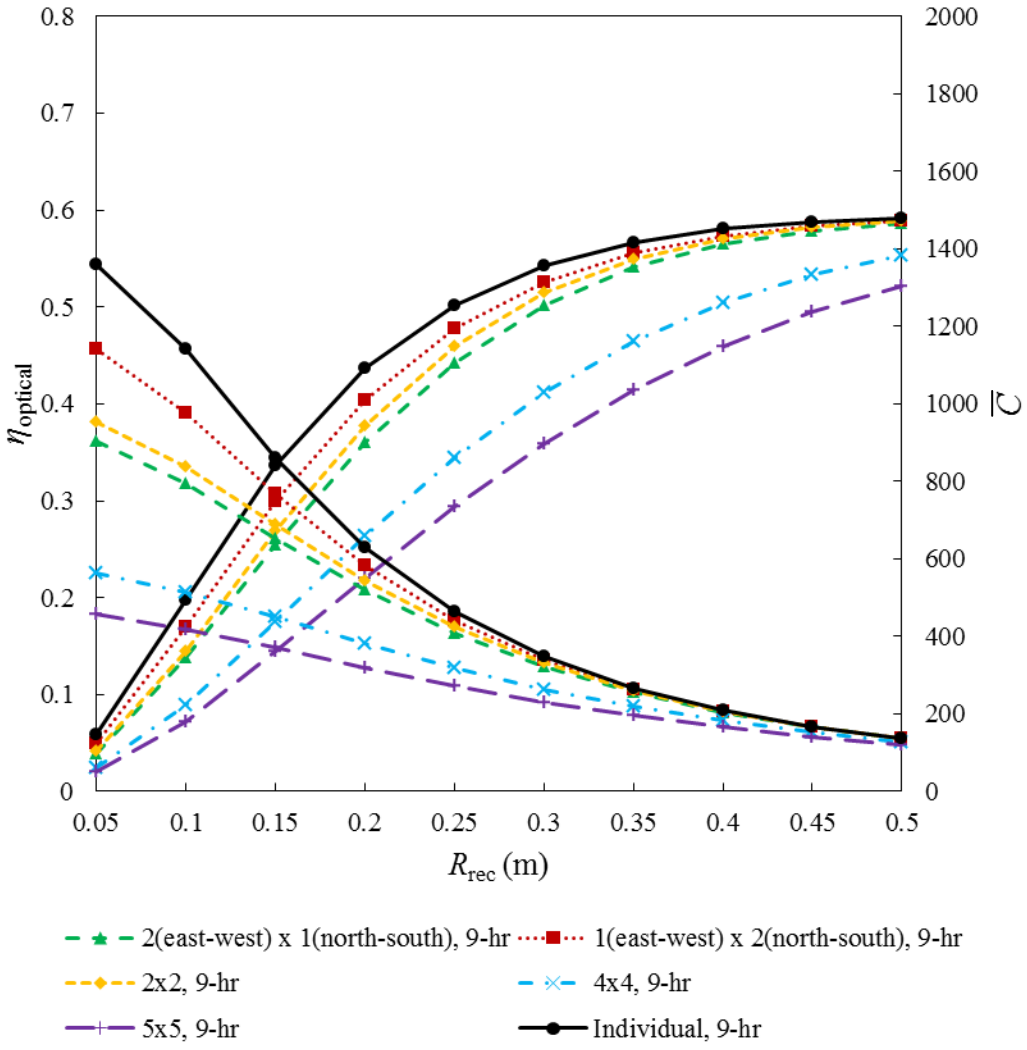

Fig. 31. Optical efficiency (left axis) and concentration ratio (right axis) for different receiver sizes and 9 hours of operation about solar noon in the month of December.

An operating time of 7 hours is chosen for the daily run-time. In combination with the 0.35 m radius size, this allows for the best linked tracking mechanism to operate at an average concentration ratio above 300 suns (315.4) and optical efficiency above 60% (60.8%) for the month of December, when the level of solar radiation is low. It is interesting to note that the daily efficiency for the TT-2x2 reflector linkage is slightly

higher than the annual efficiency for a TT-2x1 reflector linkage. Since the TT-1x2 configuration performs better than either of these, it is concluded that linking the heliostats in the north-south direction, at least for these conditions, results in reduced image aberration compared to an east-west linkage. When linking two heliostats in both directions, the performance is found to lie between the two-heliostat linkage performances, but is influenced more heavily by the poorer-performing configuration.

To observe the transient nature of the concentrator system, an hourly performance analysis is presented for the average day results of December and June in Fig. 32 and Fig. 33, using the design point receiver radius of 0.35 m.

(a)

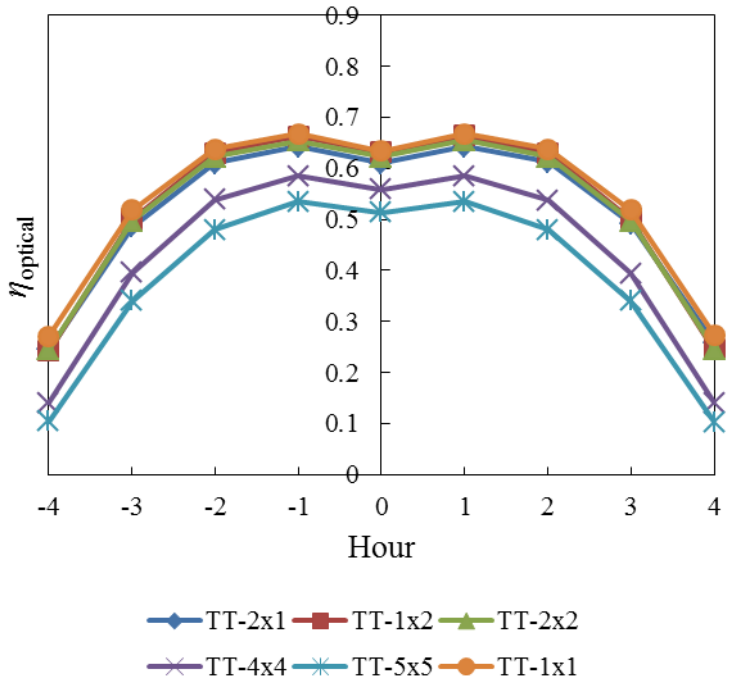

(b)

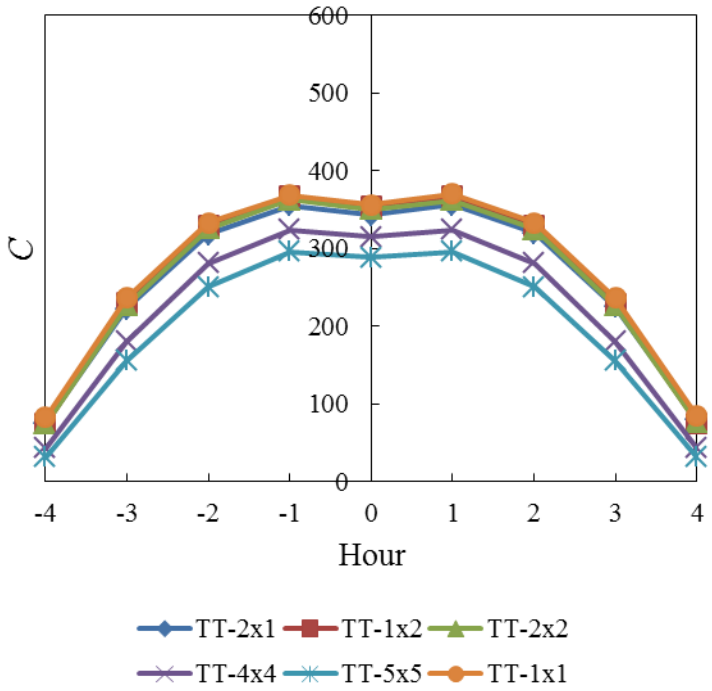

Fig. 32. Hourly (a) optical efficiency and (b) concentration ratio for the month of December.

(a)

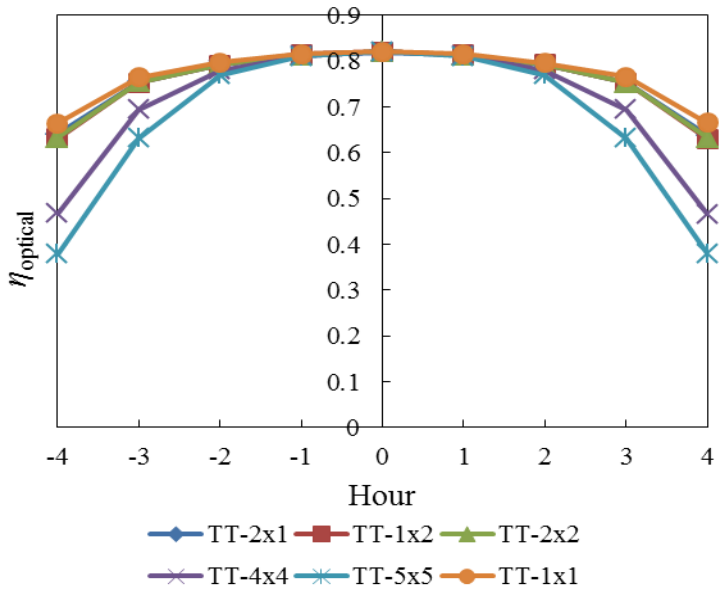

(b)

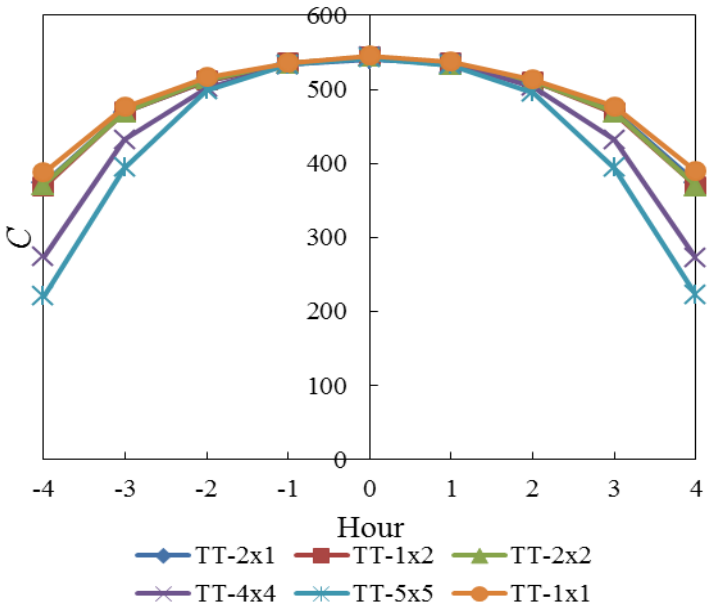

Fig. 33. Hourly (a) optical efficiency and (b) concentration ratio for the month of June.

In both cases, and in general when using the chosen solar model, the optical efficiency is symmetric about solar noon. This is due to the nature of the sun's movement and the definition that solar noon represents the time during the day when the solar azimuth angle is zero. The daily average optical efficiency throughout the year as a function of the month is obtained for each of the investigated tracking methods.

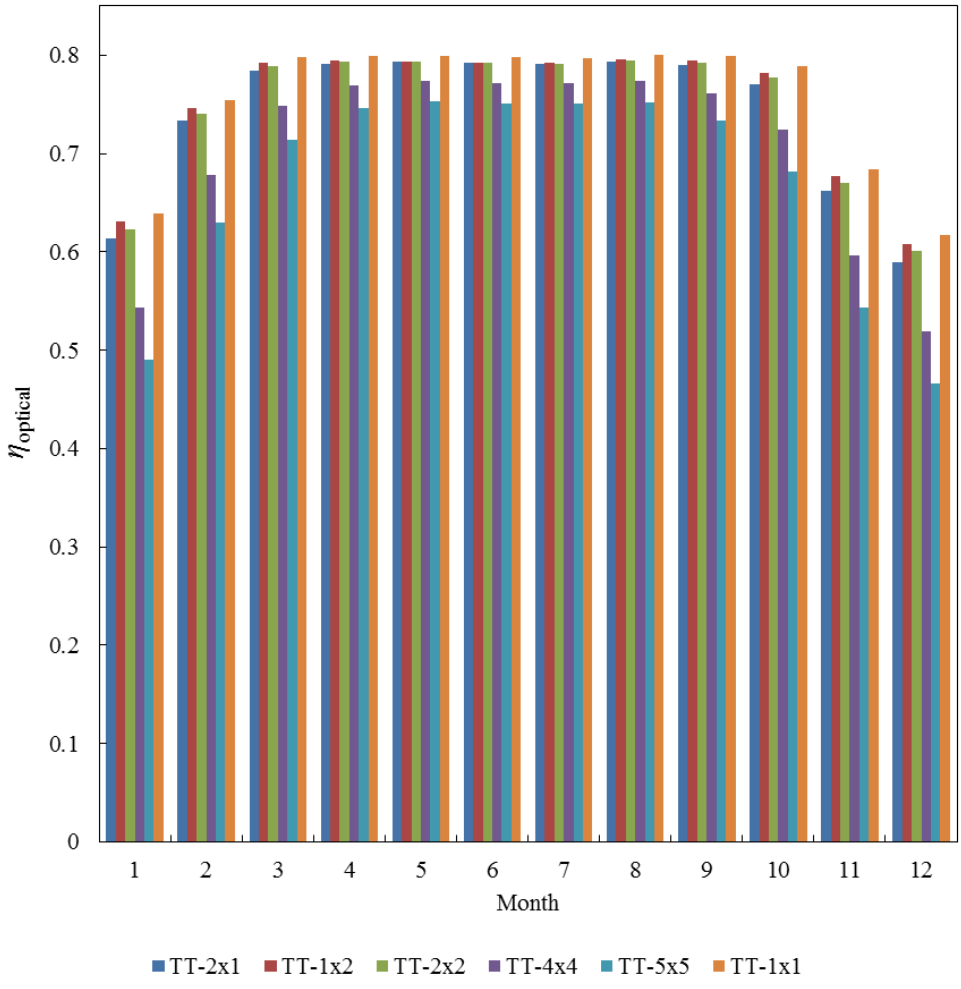

Fig. 34. Monthly-average optical efficiency $\eta_{optical}$ for the different tracking types, 7-hour operation about solar noon, and a 35-cm receiver radius.

TT-1x2 suffers the fewest losses compared to TT-1x1, and, as expected, TT-5x5 performs the worst. Typically the more heliostats that are linked, the more severe the penalty in optical efficiency far from the optimization date. The daily average concentration ratio is calculated and presented in a similar way.

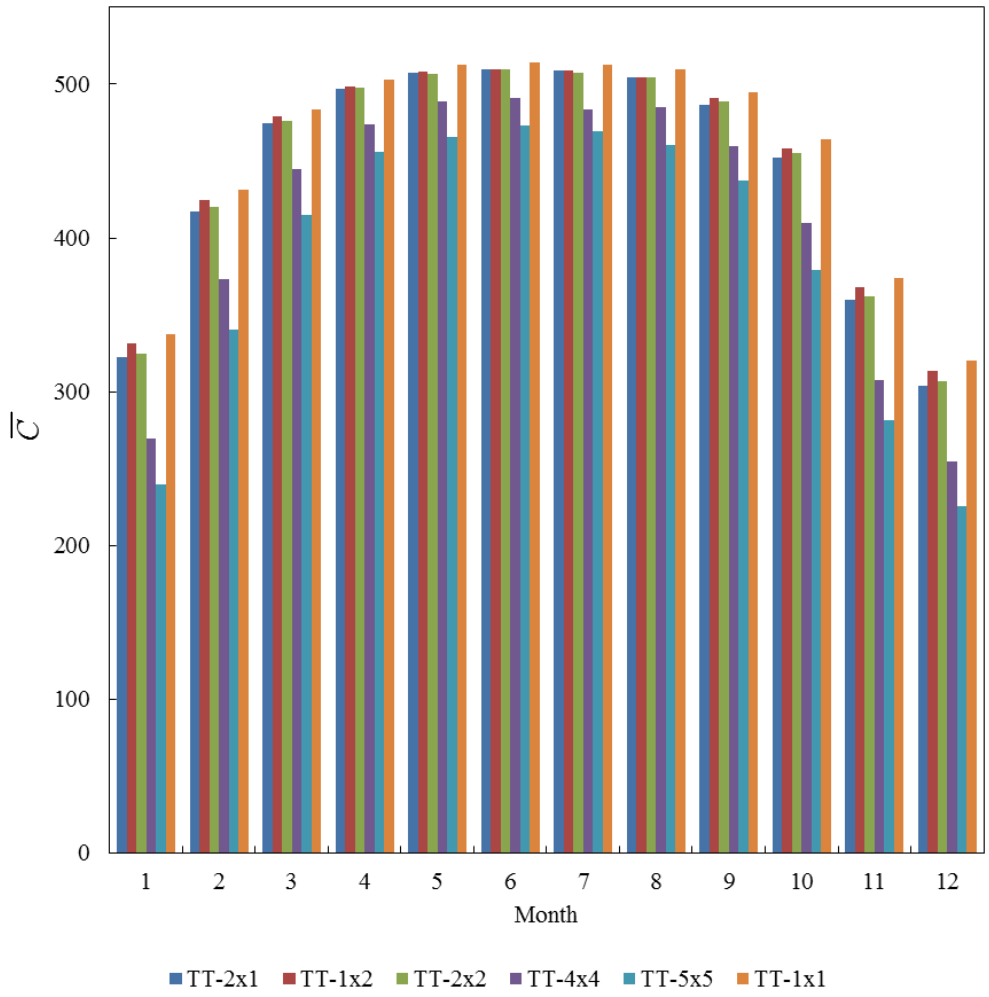

Fig. 35. Monthly-average concentration ratio for each tracking type, for 7-hour operation about solar noon and 35-cm receiver radius.

To visualize the image on the receiver plane, heat flux maps are generated using Matlab and the results of the optical simulations. The maps are created using the sum of energy striking the receiver in 5mm x 5mm square segments over the specified time. Since performance is most negatively affected in December for all tracking types, the images for each tracking type at 10:00 are shown.

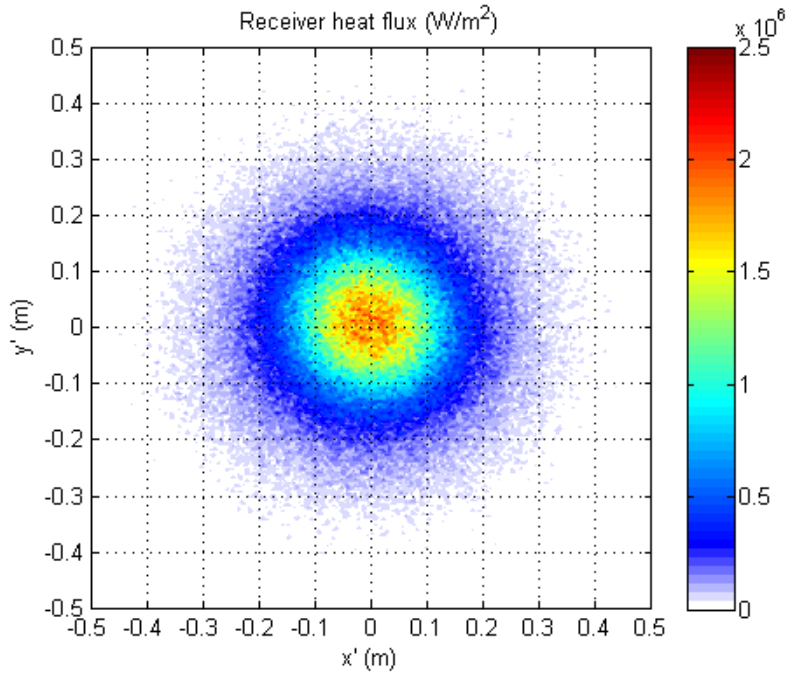

Fig. 36. TT-1x1 tracking, hour 2 (14:00) of December day simulation.

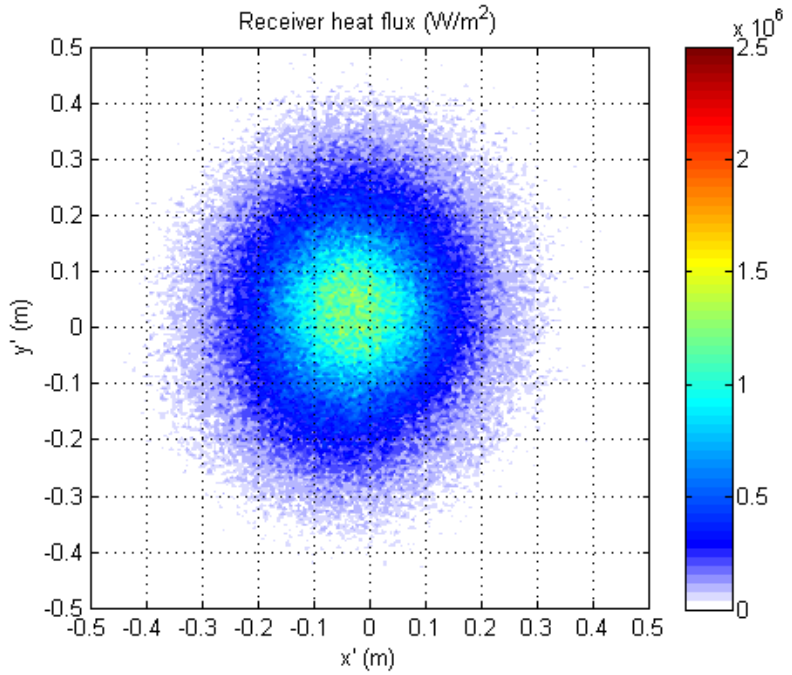

Fig. 37. TT-2x1 tracking, hour -2 (10:00) of December day simulation.

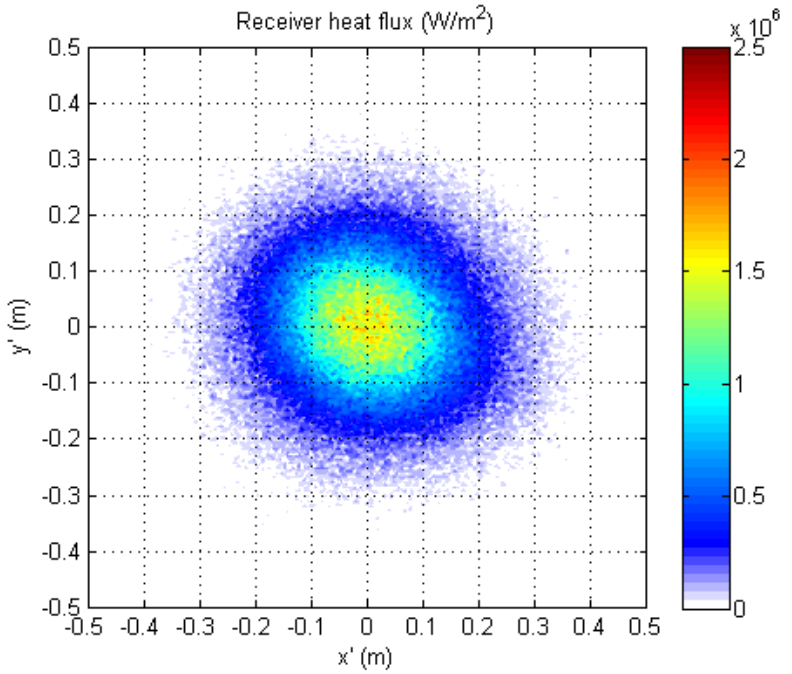

Fig. 38. TT-1x2 tracking, hour -2 (10:00) of December day simulation.

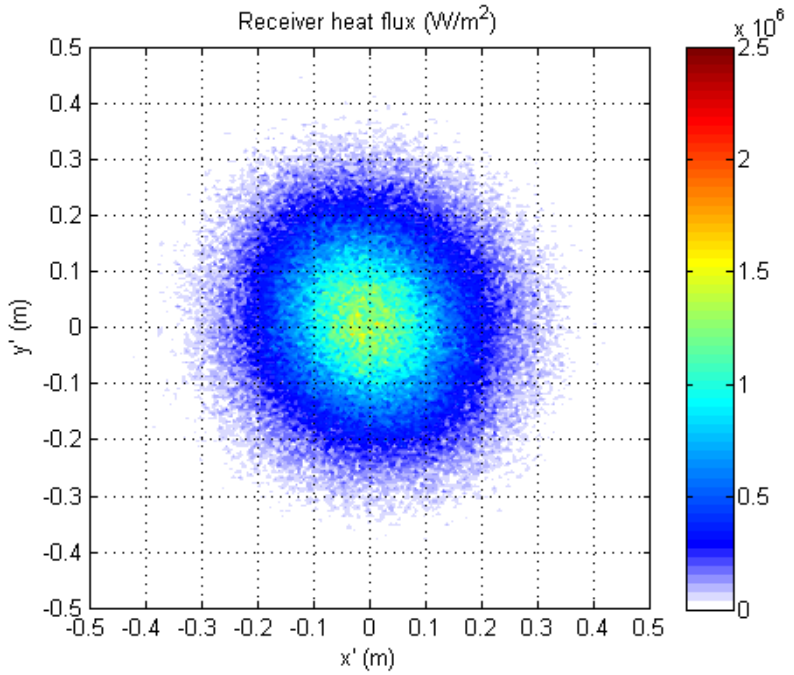

Fig. 39. TT-2x2 tracking, hour -2 (10:00) of December day simulation.

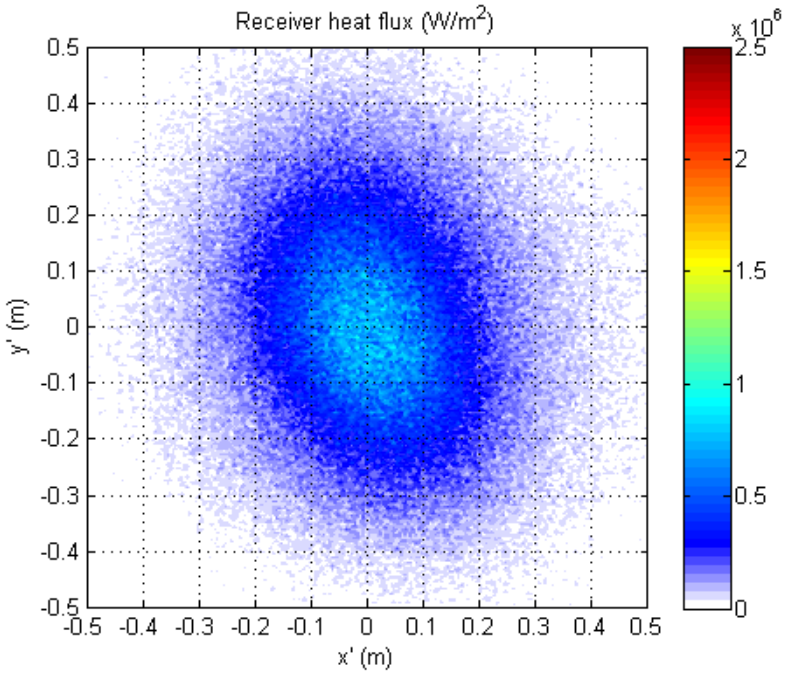

Fig. 40. TT-4x4 tracking, hour -2 (10:00) of December day simulation.

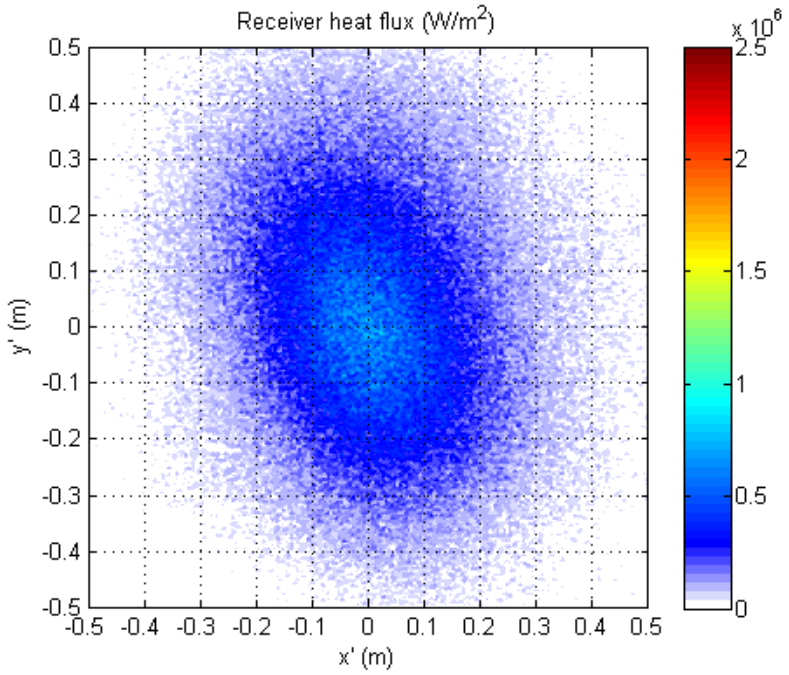

Fig. 41. TT-5x5 tracking, hour -2 (10:00) of December day simulation.

All scales are fixed to a maximum heat flux of 2.5 MW/m^2 for easier comparison. While some of the shapes may appear to be more concentrated toward the center than in the case of individual tracking, it is important to keep in mind that the minimum heat flux associated with a color is approximately 40 kW/m^2. For the larger linkages, the image does spread considerably, which causes the reduction in heat flux within the receiver area demonstrated above. The case for which each individual heliostat is allowed to track the sun freely gives the best performance, both with more concentrated heat flux and a more regular distribution on the receiver plane. Of the linked tracking cases, the TT-1x2 configuration gives the best performance. The image produced from configuration TT-

2x1 varies slightly from the centering and skew pattern seen with the other tracking types. This is attributed to the fact that linking the movement of heliostats in the east-west direction leads to less ideal matching of tilt angles than linking in the north-south direction, the effects of which are more pronounced in winter when the solar zenith angle is large compared to the optimization day. As more heliostats are linked together, the image spreads and deviates from a circular shape. The images become more skewed for the larger linkage setups at off-noon times because of the compromise in tracking accuracy of each reflector in the group.

Chapter 5. Thermodynamics

Heat engines are the basis for production of mechanical and electrical power in CSP systems, and different configurations of cycles and working fluids are considered here.

5.1. Cycle basics

Single Brayton and combined Brayton-Rankine cycles with various combinations of working fluids are considered for the conversion of delivered high-temperature heat at the receiver. In both systems, heat is transferred to a pressurized working fluid in the receiver. In both configurations, the cycle heated by the solar receiver is the Brayton cycle. The heated gas is expanded through a turbine to a lower pressure, producing mechanical work. This work is used to drive the Brayton cycle compressor, and the remainder can be used to drive an electric generator. The thermodynamic states of the single Brayton cycle are provided in Table 6. A component schematic and characteristic temperature vs. entropy diagram are shown in a and b, respectively.

Table 6. Thermodynamic states of the regenerated single Brayton cycle.

State	Process
1	Working fluid exits heat exchanger, enters compressor
2	Working fluid exits compressor, enters regenerator cold side
3	Working fluid exits regenerator cold side, enters solar receiver
4	Working fluid exits solar receiver, enters turbine
5	Working fluid exits turbine, enters regenerator hot side
6	Working fluid exits regenerator hot side, enters heat exchanger

(a)

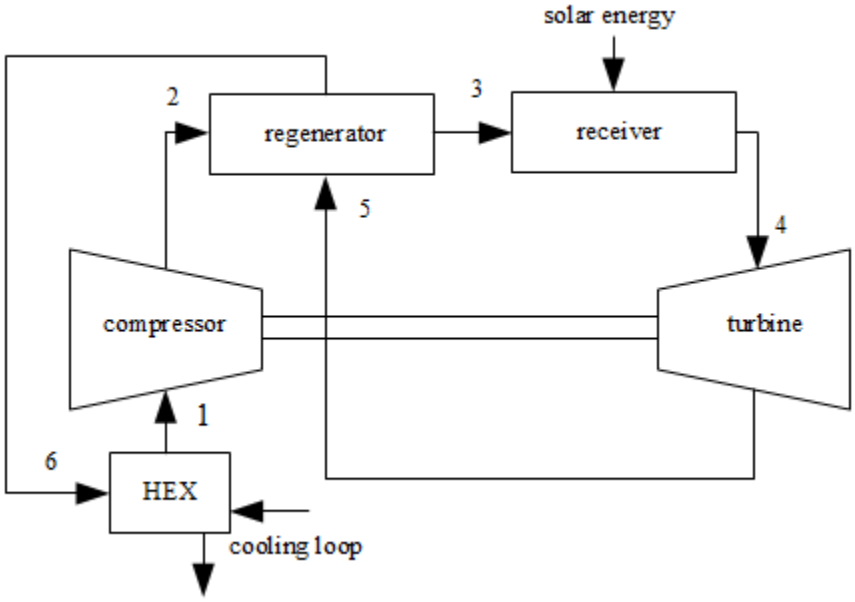

(b)

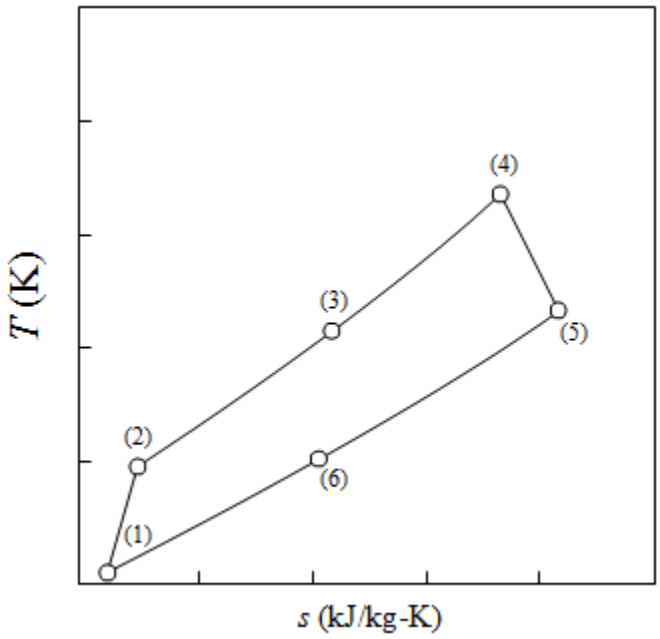

Fig. 42. (a) Component diagram and (b) T-s diagram of regenerated single Brayton cycle.

Standard thermodynamic relations for heat engine processes are used to describe different quantities of interest in the cycle. The work done by the compressor on the fluid is determined by the inlet and outlet state enthalpies and given by:

$$W_{\text{compressor}} = h_2 - h_1 \tag{28}$$

The isentropic efficiency of the compressor is found by dividing the minimum work required to compress the fluid isentropically to the actual work done on the fluid:

$$\eta_{\text{compressor}} = \frac{h_{2,s} - h_1}{h_2 - h_1} \tag{29}$$

After exiting the compressor, the working fluid enters the cold side of the regenerator for pre-heating. The effectiveness of heat recovered is defined as:

$$\varepsilon_{\text{reg}} = \frac{\text{actual heat transfer}}{\text{maximum heat that can be transferred}} = \frac{h_3 - h_2}{h_5 - h_2} \tag{30}$$

After exiting the cold side of the regenerator, the fluid enters the solar receiver. The heat rate absorbed by the working fluid is defined as:

$$\dot{Q}_{\text{useful}} = \dot{m}_{\text{top}} \left(h_4 - h_3 \right) \tag{31}$$

After exiting the receiver, the working fluid expands through the turbine, producing mechanical work:

$$W_{\text{turbine,top}} = h_4 - h_5 \tag{32}$$

The isentropic turbine efficiency is characterized similarly to the isentropic compressor efficiency, except in the case of the turbine the actual process gives a smaller enthalpy difference than does the isentropic process:

$$\eta_{\text{turbine,top}} = \frac{h_4 - h_5}{h_4 - h_{5,\text{s}}} \tag{33}$$

The energy lost by the hot fluid entering the regenerator is assumed to be the same as that gained by the cold fluid, allowing state 6 to be characterized:

$$h_5 - h_6 = h_3 - h_2 \tag{34}$$

The net power produced is calculated by taking the power produced in the turbine and subtracting the power required for the compressor:

$$P_{\text{top}} = \dot{W}_{\text{net,top}} = \dot{W}_{\text{turbine,top}} - \frac{\dot{W}_{\text{compressor}}}{\eta_{\text{shaft}}} = \dot{m}_{\text{top}} \left(\left(h_4 - h_5 \right) - \frac{\left(h_2 - h_1 \right)}{\eta_{\text{shaft}}} \right) \tag{35}$$

The cycle efficiency for heat in to mechanical work out is:

$$\eta_{\text{th,top}} = \frac{\dot{W}_{\text{net,top}}}{\dot{Q}_{\text{useful}}} = \frac{\left(h_4 - h_5 \right) - \dfrac{\left(h_2 - h_1 \right)}{\eta_{\text{shaft}}}}{h_4 - h_3} \tag{36}$$

It has been shown that lower-temperature heat such as that rejected from a Brayton cycle heat engine during cooling can be effectively used in a bottoming cycle, typically with organic working fluids [40–42]. A diagram of such a combined cycle is given in Fig. 43.

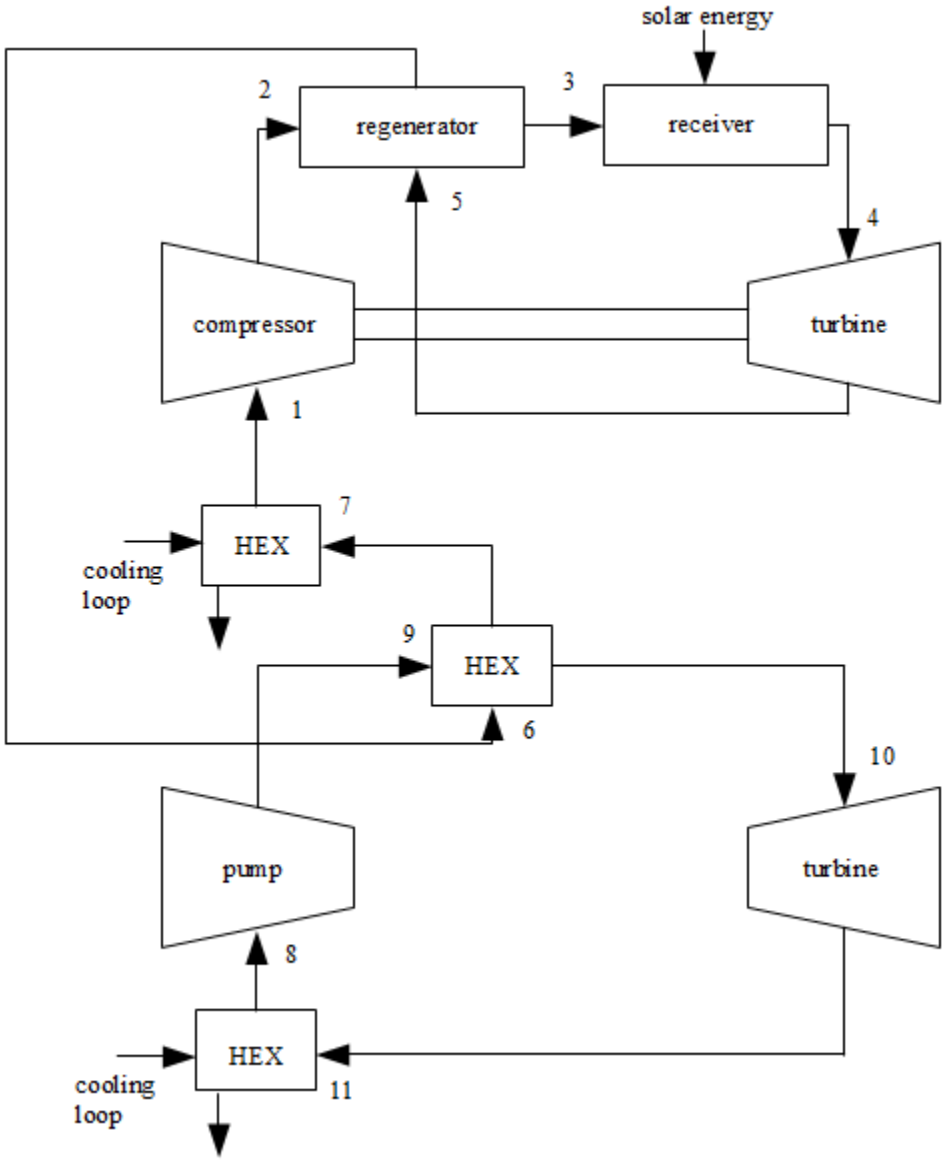

Fig. 43. Component schematic of cascading Brayton–Rankine cycle.

The bottoming cycle is typically a Rankine cycle which may operate with or without superheat. The processes of the combined Brayton–Rankine system are listed in Table 7.

Table 7. Thermodynamic states of the cascading Brayton–Rankine system.

State	Process
1	Topping fluid exits heat exchanger to ambient, enters compressor
2	Topping fluid exits compressor, enters recuperator cold side
3	Topping fluid exits recuperator cold side, enters solar receiver
4	Topping fluid exits solar receiver, enters turbine
5	Topping fluid exits turbine, enters recuperator hot side
6	Topping fluid exits recuperator hot side, enters heat exchanger to bottoming cycle
7	Topping fluid exits heat exchanger to bottoming cycle, enters heat exchanger to ambient
8	Bottoming fluid exits heat exchanger to ambient, enters pump
9	Bottoming fluid exits pump, enters heat exchanger cold side
10	Bottoming fluid exits heat exchanger, enters turbine
11	Bottoming fluid exits turbine, enters heat exchanger to ambient

To analyze the thermodynamics of the combined system, the heat supplied to the bottoming cycle must be determined. Due to the phase change of the bottoming cycle fluid, this becomes a pinch point problem. The pinch point represents the minimum temperature difference found across the length of heat exchange, and occurs when the bottoming cycle fluid reaches the saturation temperature with a fluid quality of 0%. The percentage of heat used to bring the bottoming cycle fluid from the saturated liquid state to the superheated turbine inlet state is the same as the percentage of heat used to bring the topping cycle fluid from the heat exchanger inlet state to the pinch point. This can be expressed as:

$$\frac{h_{10} - h_{\text{bottom,pinch}}}{h_{10} - h_9} = \frac{h_6 - h_{\text{top,pinch}}}{h_6 - h_7} \tag{37a}$$

$$\dot{m}_{\text{top}}\left(h_6 - h_7\right) = \dot{m}_{\text{bottom}}\left(h_{10} - h_9\right) \tag{37b}$$

The net power delivered by the bottoming cycle is the turbine power minus the required pump power:

$$P_{\text{bottom}} = \dot{m}_{\text{bottom}}\left(\left(h_{10} - h_{11}\right) - \left(h_9 - h_8\right)\right) \tag{38}$$

The overall thermal efficiency of the combined cycle is then:

$$\eta_{\text{th,combined}} = \frac{P_{\text{top}} + P_{\text{bottom}}}{\dot{Q}_{\text{useful}}} \tag{39}$$

Four primary working fluids are considered for the Brayton cycle based on their previous use in Brayton cycles and also for CSP applications in general: air [42], CO_2 [42], He [8], and H_2 [47]. Engineering Equation Solver [30] is used to solve the thermodynamic equations with its simultaneous equation solver and library of thermodynamic property data. Table 8 provides a list of each of the Brayton cycle fluids, thermodynamic data references used by EES, and applicable temperature range of the thermodynamic models.

Table 8. Working fluids considered for use in Brayton cycle.

Fluid	Reference	T range (K)
Air	[48] as cited by [30]	$60 < T < 2000$
CO_2	[49] as cited by [30]	$216.6 < T < 1100$
He	[50] as cited by [30]	$2.1768 < T < 1500$
H_2	[51])] as cited by [30]	$13.957 < T < 1000$

A list of organic fluids is considered for operation as the working fluid in the bottoming cycle. Table 9 provides a list of each of the considered bottoming Ranking cycle working

fluids, thermodynamic data references, and applicable temperature range of the thermodynamic models.

Table 9. Working fluids considered for use in bottoming Rankine cycle.

Fluid	Reference	T range (K)
C6-Fluoroketone	[30]	not provided
Cyclohexane	[52] as cited by [30]	$279.5 < T < 700$
HFE7000	[30]	$230 < T < 438$
n-Pentane	[53] as cited by [30]	$177 < T < 589$
R-141b	[54] as cited by [30]	not provided
R-245fa	[55] as cited by [30]	$175 < T < 440$

5.2. The solar receiver

The thermal efficiency is dependent upon the highest achievable temperature in the working fluid, which in the case of a solar receiver, is dependent upon the concentrated heat flux. To determine the relationship between concentration ratio and fluid temperature, an energy balance is constructed. An illustration is provided in Fig. 44.

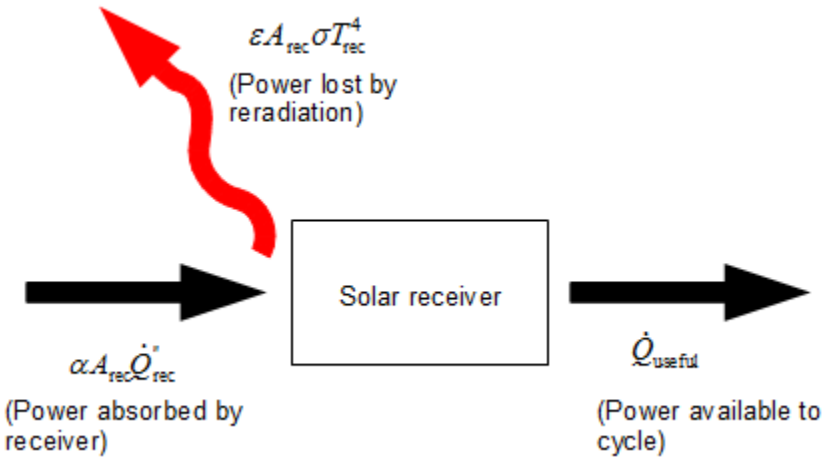

Fig. 44. Energy balance diagram for solar receiver.

$$\dot{Q}_{useful} = \dot{Q}_{absorbed} - \dot{Q}_{lost} = \alpha A_{rec} q''_{rec} - \varepsilon A_{rec}\sigma T_{rec}^4 \tag{40}$$

The heat flux at the receiver is known from the Monte Carlo ray tracing analysis. The absorptivity and emissivity of a cavity-type receiver has been shown to closely approximate a black body [43], therefore their values are assumed to be equal to unity. Since re-radiation typically dominates other losses in high temperature receivers [44], it is assumed that the receiver is perfectly insulated and all losses are due to re-radiation. Both the useful heat rate available to the cycle and the receiver temperature can be related to the heat flux incident on the receiver by assuming a receiver efficiency, relating the amount of power absorbed into the thermodynamic cycle to the amount of total power incident on the receiver. A receiver efficiency of 70% is assumed as the nominal value for analysis. The receiver is assumed to be perfectly insulated with losses only due to re-radiation.

$$\eta_{rec} = \frac{\dot{Q}_{useful}}{A_{rec}\dot{Q}''_{rec}} = \frac{\dot{m}(h_4 - h_3)}{A_{rec}\dot{Q}''_{rec}} = \frac{\alpha A_{rec} q''_{rec} - \varepsilon A_{rec}\sigma T_{rec}^4}{A_{rec}\dot{Q}''_{rec}} = \alpha - \varepsilon\frac{\sigma T_{rec}^4}{\dot{Q}''_{rec}} \tag{41a}$$

$$T_{rec} = \left(\frac{q''_{rec}}{\varepsilon\sigma}(\alpha - \eta_{rec})\right)^{1/4} \tag{41b}$$

$$\dot{Q}_{useful} = \eta_{rec} A_{rec} q''_{rec} \tag{41c}$$

Unfortunately, accurately calculating the attainable fluid temperature from the receiver temperature is not trivial. Most simply, two limiting cases can be considered. The first is the assumption of a constant receiver-fluid temperature difference, which is the most optimistic case. However, this implies that for increasing levels of heat transfer, such as would be expected from increasing concentration ratios approaching solar noon, the overall heat transfer coefficient must increase proportionally. While the heat transfer coefficient could potentially increase due to increased turbulence from higher mass flow rates, it is unlikely that the change would be controllable to match the heat transfer and sustain the constant temperature difference. The second limiting case is that of constant fluid temperature. This is the most pessimistic case, as an increase in heat transfer would not contribute to sensible heating of the working fluid. In the absence of a specific and detailed receiver analysis which is beyond the scope of this thesis, an assumption is made based on reported performances of different solar receivers. A review paper by Avila-Marin [11] reports a mean experimental outlet air temperature, flux, and receiver efficiency for a variety of small solar gas receivers. Assuming that these efficiencies can be used to calculate a mean experimental receiver temperature from Eq. (41b), an estimated receiver-fluid temperature difference can be calculated for each reported

receiver.

$$\Delta T_{\text{rec-fluid,exp}} = \left(\frac{q''_{\text{rec,exp}}}{\varepsilon\sigma} \left(\alpha - \eta_{\text{rec,exp}} \right) \right)^{1/4} - T_{\text{fluid,exp}} \tag{42}$$

A plot is constructed from the reported experimental data for a selection of receivers and is shown in Fig. 45.

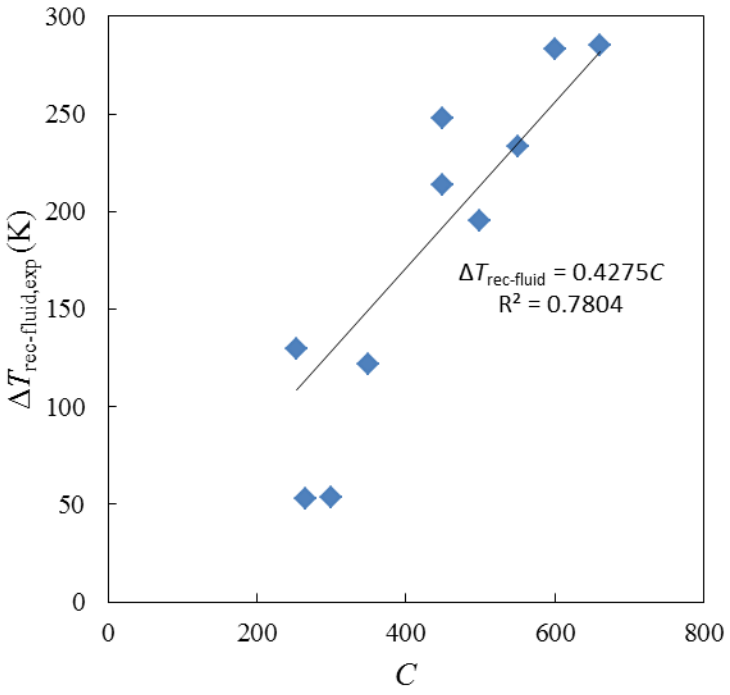

Fig. 45. Estimated receiver–fluid temperature difference vs. concentration ratio for small gas receivers, constructed using Eq. (42) and data from [11].

Using an assumed 70% efficiency for the present analysis, the fluid temperature can now be estimated as a function of the concentration ratio.

$$T_4 = \left(\frac{\left(1000 \text{ W m}^{-2}\right) C}{\varepsilon\sigma} \left(\alpha - \eta_{\text{rec}} \right) \right)^{1/4} - \left(0.4275 \frac{\text{K}}{\text{sun}} \right) C \tag{43}$$

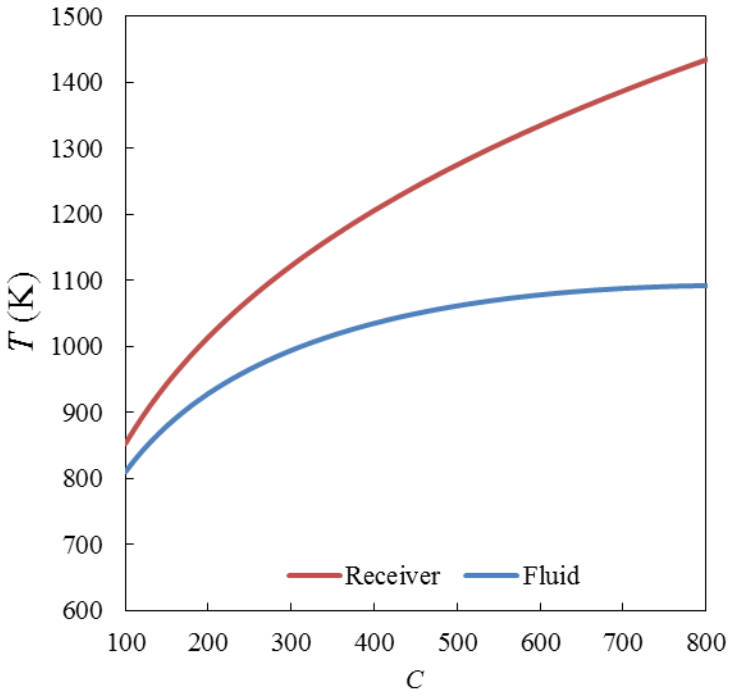

Fig. 46. Calculated receiver and fluid temperatures for varying concentration ratios.

Estimated receiver and fluid temperatures as a function of the concentration ratio are illustrated in Fig. 46 as calculated from Eqs. (41b) and (43). This approach produces a relationship that is physically intuitive over the range of expected concentration ratios and in between the two limiting cases of temperature difference assumption.

The overall system efficiency is expressed as:

$$\eta_{\text{system}} = \eta_{\text{optical}} \eta_{\text{rec}} \eta_{\text{th}} \tag{44}$$

where η_{th} is the single or combined-cycle thermal efficiency.

After performing the optical analysis, the calculated efficiencies, thermal powers, and concentration ratios are used as inputs to the thermodynamic simulations to determine

overall system performance. For the Brayton cycle, component efficiencies of the compressor, turbine, and regenerator follow those used by Galanti, et al. [24] for a 50 kWe gas microturbine with regeneration based on a test unit operating at the University of Genoa. These values are a compressor efficiency of 0.796, a turbine efficiency of 0.858, and a regenerator effectiveness of 0.87. In the simulation, the mass flow rate is varied to account for the time-dependent heat input and fluid temperature driven by the receiver heat flux. For simplicity and for lack of available data specific to this unit, it is assumed that the isentropic component efficiencies remain constant during operation and for pressure ratios between 2–4. It is assumed that there is inefficiency from pressure loss present in the system. The components through which pressure loss is assumed to occur are the heat exchangers, including the Brayton cycle regenerator, the solar receiver, the heat exchanger between the topping and bottoming cycles, and the heat exchangers to ambient. A 5% pressure loss is assumed in the solar receiver. A 2% pressure loss is assumed in all other components. The pressure loss is expressed in relative terms, so that the fluid pressures at the inlet and outlet of the solar receiver are related by:

$$0.97\, p_3 = p_4 \tag{45}$$

When a combined cycle is considered, the turbine inlet temperature of the bottoming cycle fluid is assumed to be able to reach a temperature 40 K below the temperature of the topping cycle fluid at state 6, the inlet to the hot side of the heat exchanger between the topping and bottoming cycles. This is a conservative estimate compared to the work of Marrero, et al. [45] which assumes a 30 K temperature difference between the gas

turbine exhaust and steam superheater exit in a combined cycle. The pinch point temperature difference is fixed to 10 K for this analysis. The isentropic pump and turbine efficiencies for the bottoming cycle are taken as 0.5 (assumed) and 0.452 [46], respectively. These values are assumed to be representative of the small system analyzed here and are lower than those of larger ORC components, thereby leading to potentially conservative calculations.

5.3. Single Brayton cycle operation

Using daily-average heat flux and efficiency from the case of individually-tracking heliostats as inputs to the single Brayton cycle thermodynamic simulation, the pressure ratio p_R is varied between 2.0–4.0, with a low pressure at 0.1 MPa, to determine the operating pressure ratio for each of the four Brayton cycle fluids. The results are shown for the months of December and June.

(a)

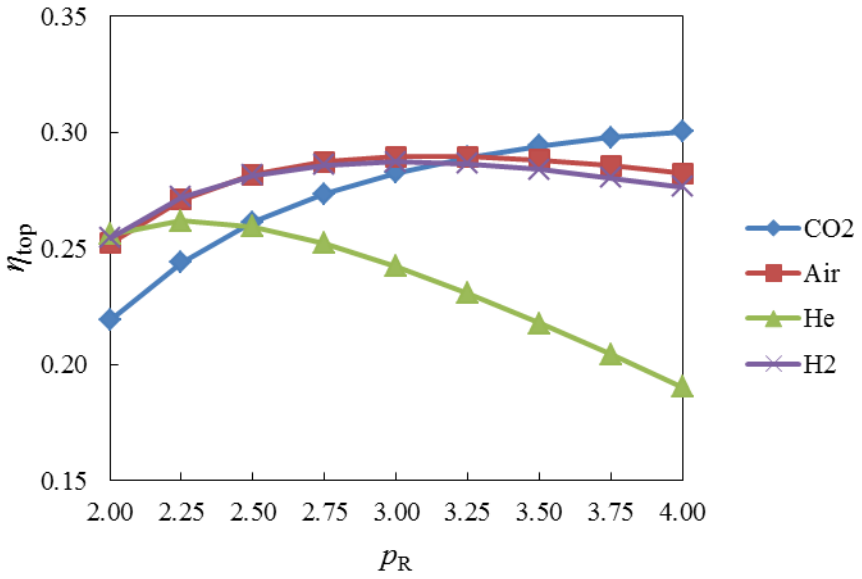

(b)

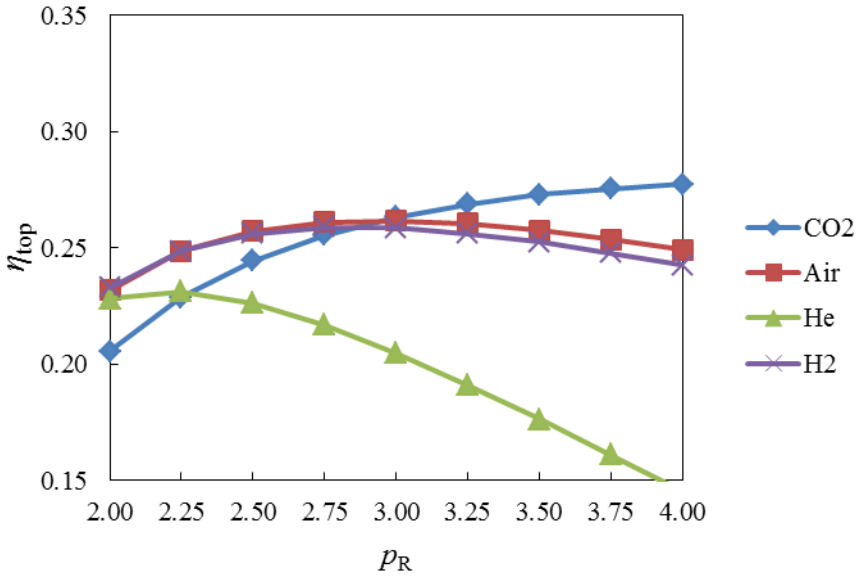

Fig. 47. Brayton cycle efficiency as a function of pressure ratio for selected working fluids in (a) December, and (b) June for 7 hour operation, 35 cm receiver radius, and TT-1x1 heliostat tracking.

The optimal pressure ratio and resulting average cycle efficiency for the months of December and June for each working fluid is given in Table 10.

Table 10. Optimal pressure ratio and resulting average cycle efficiency for December and June for each working fluid considered in the single Brayton cycle.

	p_R	C_{Dec}	C_{Jun}	$\eta_{optical,Dec}$	$\eta_{optical,Jun}$	$\eta_{top,Dec}$	$\eta_{top,Jun}$
Air	3.0	319.6	514.8	0.617	0.798	0.262	0.290
CO_2	4.0	319.6	514.8	0.617	0.798	0.277	0.300
He	2.25	319.6	514.8	0.617	0.798	0.231	0.262
H_2	3.0	319.6	514.8	0.617	0.798	0.259	0.287

It is assumed that the use of the daily average concentration ratio is acceptable to characterize the daily input to the thermodynamic cycle for the annual simulation. A comparison of CO_2 Brayton cycle efficiencies in June using hourly and average concentration ratio input is shown in Fig. 48.

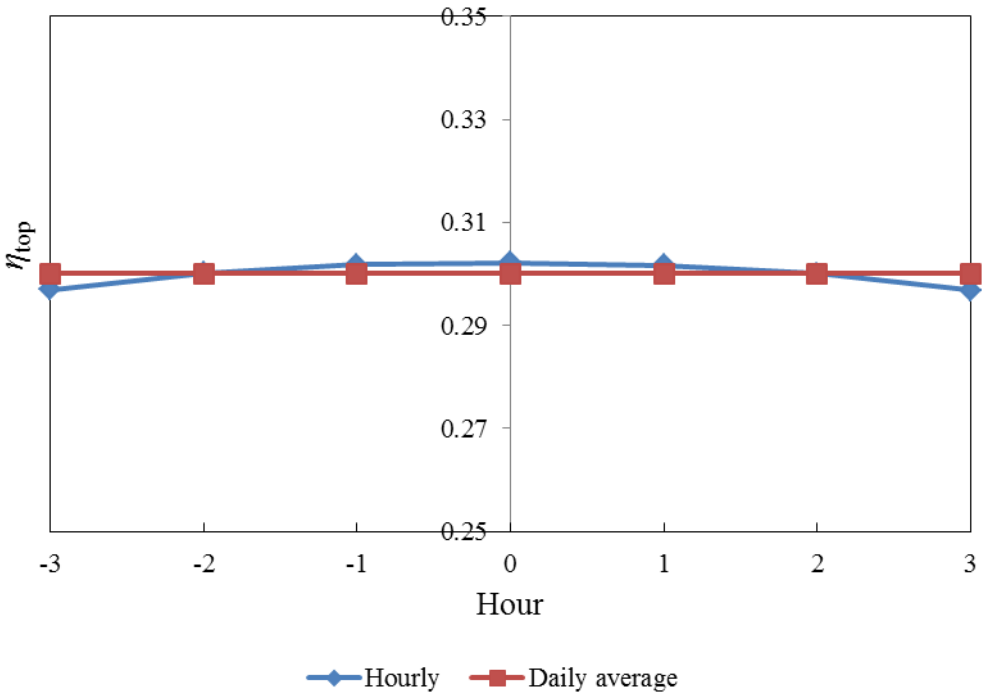

Fig. 48. Comparison of June Brayton cycle efficiency for hourly and 7 hour daily average concentration ratio input.

It is assumed reasonable to use the daily-average concentration ratio as input to the annual thermodynamic analysis based on the similarity of the efficiency curves in Fig. 48. Average daily cycle efficiency η_{cycle} is given as a function of the month for each of the considered tracking configurations when using air (Fig. 49a), CO_2 (Fig. 49b), He (Fig. 49c), and H_2 (Fig. 49d).

(a)

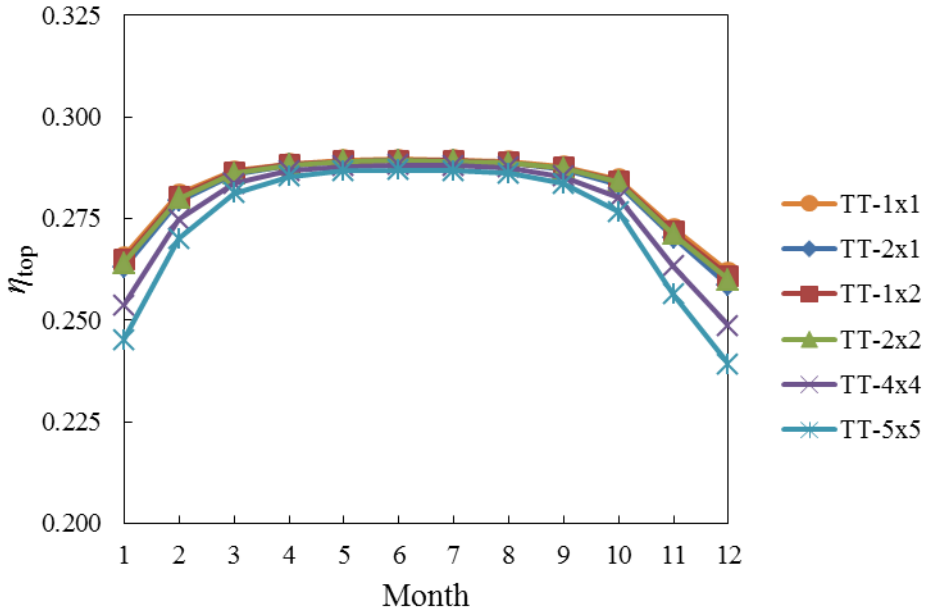
0.325
0.300
0.275
0.250
0.225
0.200
η_{top}
1
2
3
4
5
6
7
8
9
10
11
12
Month
TT-1x1
TT-2x1
TT-1x2
TT-2x2
TT-4x4
TT-5x5

(b)

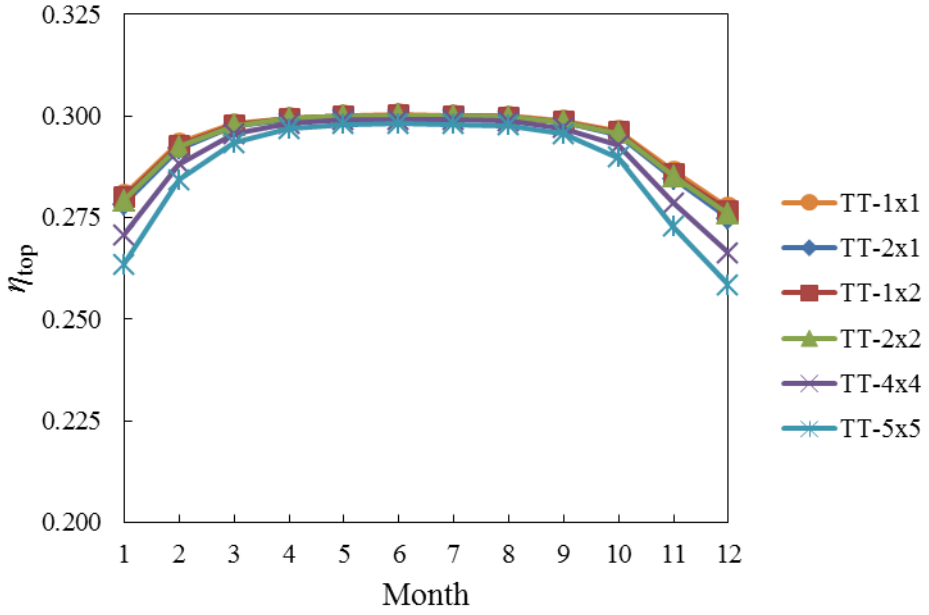
0.325
0.300
0.275
0.250
0.225
0.200
η_{top}
1
2
3
4
5
6
7
8
9
10
11
12
Month
TT-1x1
TT-2x1
TT-1x2
TT-2x2
TT-4x4
TT-5x5

(c)

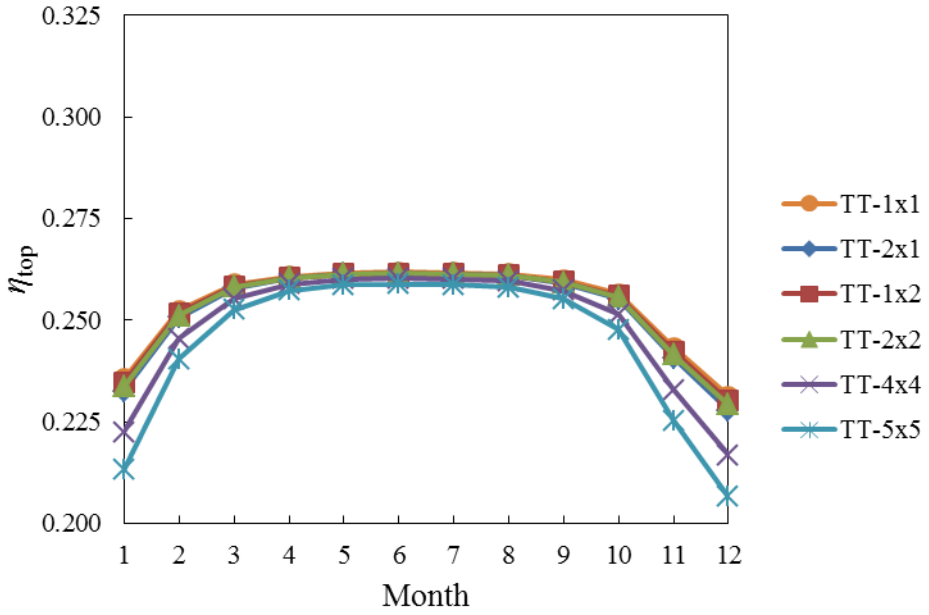

(d)

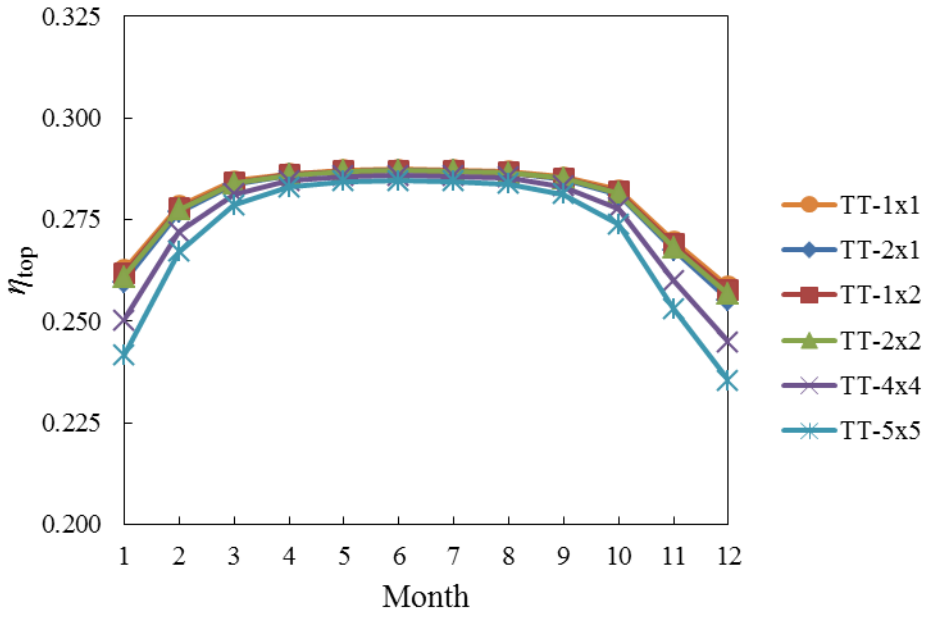

Fig. 49. Average monthly single Brayton cycle efficiency as a function of month for each tracking type, using (a) air, (b) CO_2, (c) He, or (d) H_2.

The results of Fig. 49 show that a single Brayton cycle operating with CO_2 as the working fluid provides superior performance. Furthermore, when using linked tracking, all cycles perform the best when fed by the TT-1x2 configuration. This is due to the increased average concentration ratio, which increases the maximum temperature seen in the thermodynamic cycle. The peak cycle efficiency for CO_2 and the aforementioned linkage system occurs in June, with a thermodynamic efficiency of 0.300. The lowest efficiency occurs in December, with a value of 0.277. The monthly average solar-to-electric efficiency, assuming an electric generator efficiency of 0.97, when using TT-1x2 and CO_2 in a single Brayton cycle is plotted in Fig. 50.

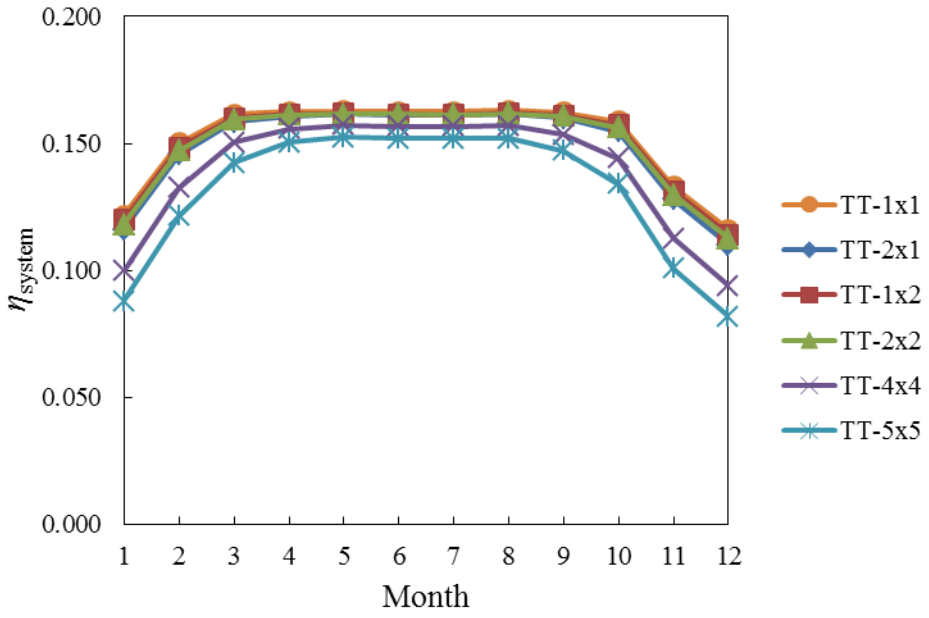

Fig. 50. Monthly average solar-to-electric (total system) conversion efficiency for single CO_2 Brayton cycle and different tracking types.

The peak average solar-to-electric conversion efficiency for a linked tracking heliostat configuration is found to be 0.162 for the TT-1x2 setup. Implementing the TT-1x2 tracking system leads to a maximum 1.64% reduction in system efficiency for the month of December. The worst-performing option is the TT-5x5 tracking, which leads to a 29.5% reduction in system efficiency in December.

5.4. Combined Brayton–Rankine cycle operation

A combined Brayton-Rankine cycle is then analyzed. Since the CO_2 cycle performs the best of all other fluids considered for the Brayton cycle, it is chosen as the topping cycle fluid. The optimum maximum pressure is chosen for each bottoming organic fluid by changing the maximum pressure of the cycle until the power output from the bottoming cycle, and therefore the combined cycle efficiency, reaches a maximum. The solar input datum is taken as the average daily input for the month of June from the case of individual heliostat tracking. The results are provided in Table 11.

Table 11. Average June operation for combined cycle topped with CO_2 Brayton cycle.

	$p_{min,bottom}$ (MPa)	$p_{max,bottom}$ (MPa)	P_{top} (kW)	η_{top}	P_{bottom} (kW)	η_{bottom}	$P_{combined}$ (kW)	$\eta_{combined}$
C6-Fluoroketone	0.1	0.8	41.66	0.300	2.02	0.036	43.67	0.315
Cyclohexane	0.1	0.6	41.66	0.300	2.30	0.049	43.96	0.317
HFE-7000	0.1	1.0	41.66	0.300	3.26	0.057	44.92	0.324
n-Pentane	0.1	1.2	41.66	0.300	4.18	0.074	45.84	0.331
R-141b	0.1126	1.0	41.66	0.300	4.23	0.075	45.89	0.331
R-245fa	0.2109	2.0	41.66	0.300	5.19	0.067	46.84	0.340

The working fluid R-245fa is determined to be the best-performing bottoming cycle fluid and is chosen for use in the combined cycle. The total solar-to-electric conversion efficiency for each tracking type as a function of the month is shown in Fig. 51.

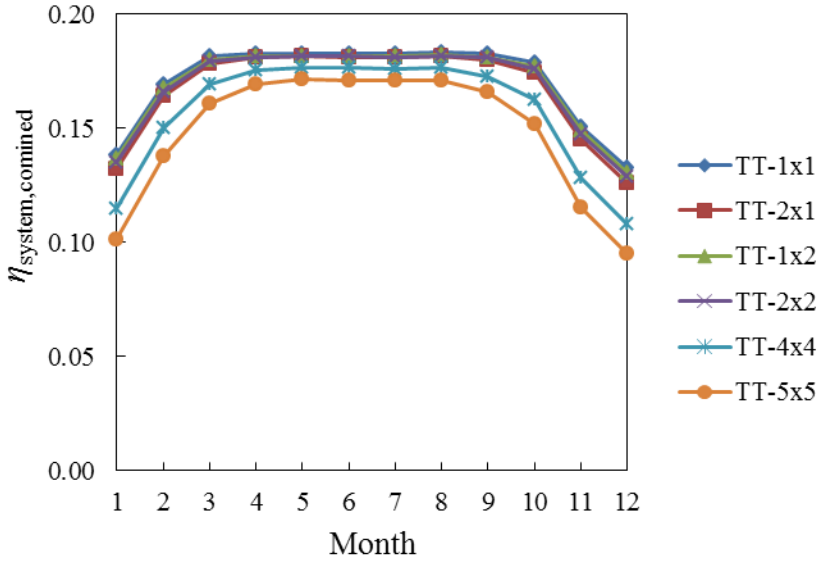

Fig. 51. Monthly average solar-to-electric conversion efficiency for combined CO_2–R-245fa cycle and different tracking types.

The peak daily system efficiency for the CO_2–R-245fa combined cycle is 18.2% when driven by the TT-1x2 linkage configuration.

Chapter 6. Economic aspects

As the drive mechanism constitutes a significant portion of overall heliostat cost [23], utilizing a linkage mechanism to drive multiple heliostats with a single drive has the potential to greatly reduce the capital cost of the optical concentration system. Using a price breakdown of components of large heliostats and assuming that the costs of individual components scale to the breakdown of small heliostats, the cost factor of linking multiple heliostats can be estimated. The direct cost estimates by component of glass-metal heliostats at different manufacturing quantities is given by Kolb et al. [23] and is outlined in Table 12.

Table 12. Cost breakdown estimate for two different heliostat types and different manufacturing quantities [23].

Component	Glass/Metal Heliostat Price @ 50,000/yr ($/m^2)	Glass/Metal Heliostat Price @ 5,000/yr ($/m^2)
Mirror Module	$23.06	$26.50
Support Structure	$21.21	$23.32
Drive	$27.11	$48.65
Drive Electrical	$1.78	$2.09
Drive Controls	$1.94	$2.67
Pedestal	$16.96	$18.66
Total Direct Cost	$92.06	$121.89

Assuming that the drive, drive electrical, and controls costs can be scaled by the ratio of heliostats to drives in the linkage system, the cost factor can be determined as a function of heliostat-to-drive ratio (*HDR*), which is defined as the number of heliostats controlled by a single drive. The concentrator cost factor is defined to be the cost of an individual

heliostat with drive costs adjusted by the heliostat-to-drive ratio divided by the cost factor with *HDR*=1.

$$F_{\text{cost,optical}} = \frac{CC_{\text{mirror}} + CC_{\text{support}} + \left(CC_{\text{drive}} + CC_{\text{electrical}} + CC_{\text{controls}}\right) / HDR + CC_{\text{pedestal}}}{CC_{\text{mirror}} + CC_{\text{support}} + CC_{\text{drive}} + CC_{\text{electrical}} + CC_{\text{controls}} + CC_{\text{pedestal}}} \tag{46}$$

Data used in Eq. (46) are taken from Table 12. Taking the typical assumption that the optical concentration system accounts for about 50% of the overall capital cost [3,4], the system cost factor is plotted as a function of HDR.

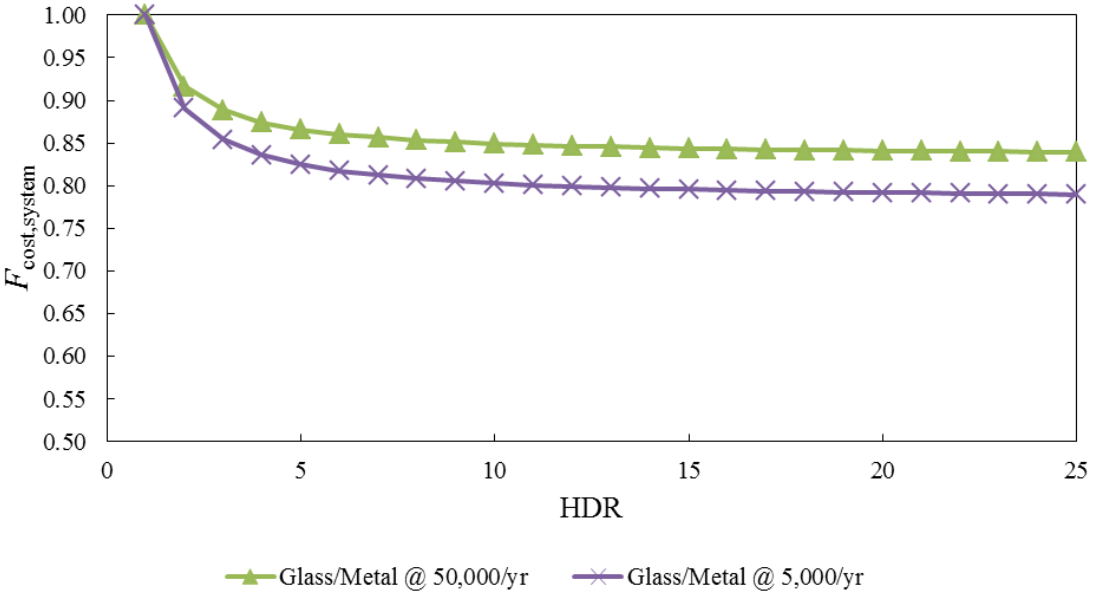

Fig. 52. Plant cost factor vs. heliostat-to-drive ratio for two different types of heliostats at two different manufacturing quantities.

Figure 52 shows a significant impact on the cost factor for a relatively small heliostat-to-drive ratio, with diminishing benefits beyond approximately 10:1. For the annual analysis, a field of 20x20 heliostats is analyzed with linked sections of ratio 2:1 (linked in the east-west direction or in the north-south direction), 4:1 (2x2 square sections), 16:1

(4x4 square sections), and 25:1 (5x5 square sections). Compared to a simulation of all heliostats tracking independently, it is assumed that in order to be practical for consideration in terms of capital cost, the decrease in performance of the system must be no more than the decrease in cost. The performance factor is defined as the ratio of system efficiency with linked tracking to the system efficiency with individual tracking:

$$F_{\text{performance}} = \frac{\eta_{\text{system,linkage}}}{\eta_{\text{system}}} \tag{47}$$

System performance and cost factors are compared for each number of grouped heliostats in Figs. 53–56 The cost factors are compared for glass-metal heliostats at either 5,000 or 50,000 units/year production.

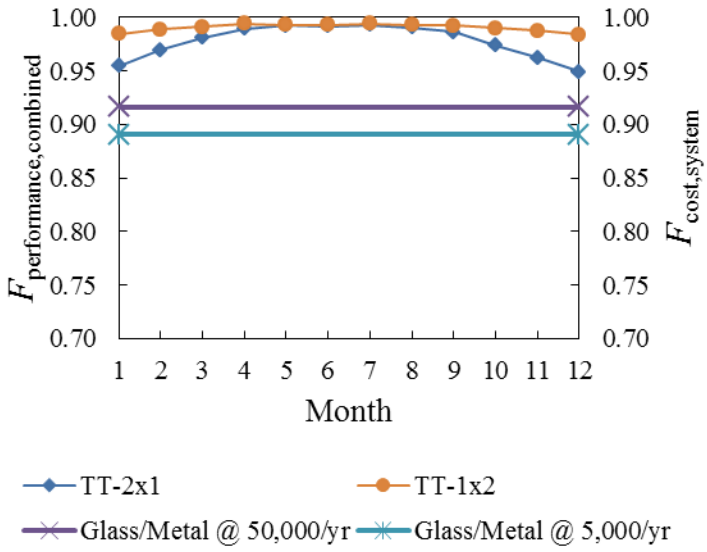

Fig. 53. Plot of cost factor (straight lines, right axis) and performance factor (curved lines, left axis) for 2-heliostat linkage simulations.

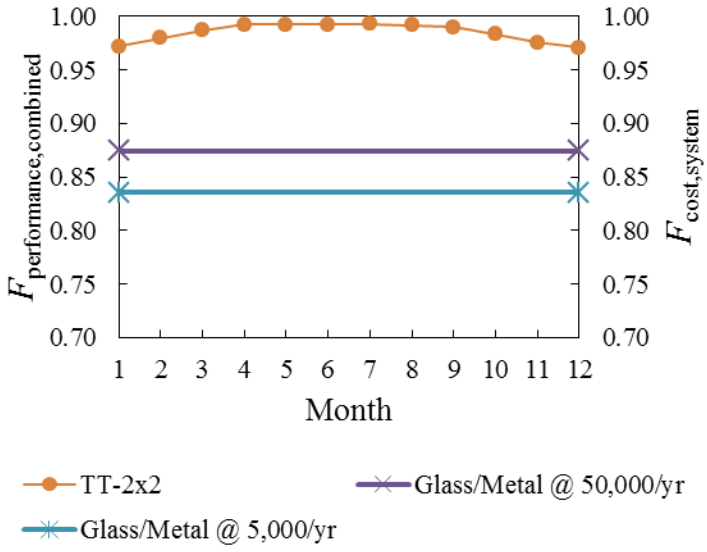

Fig. 54. Plot of cost factor (straight lines, right axis) and performance factor (curved lines, left axis) for 4-heliostat linkage simulations.

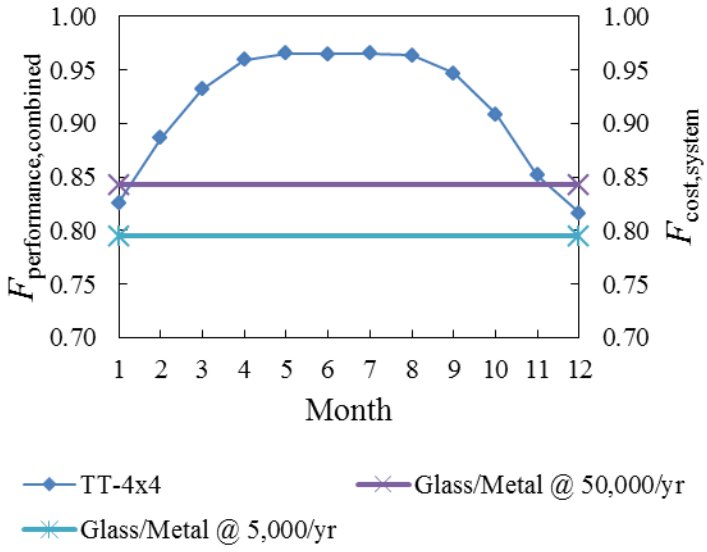

Fig. 55. Plot of cost factor (straight lines, right axis) and performance factor (curved lines, left axis) for 16-heliostat linkage simulations.

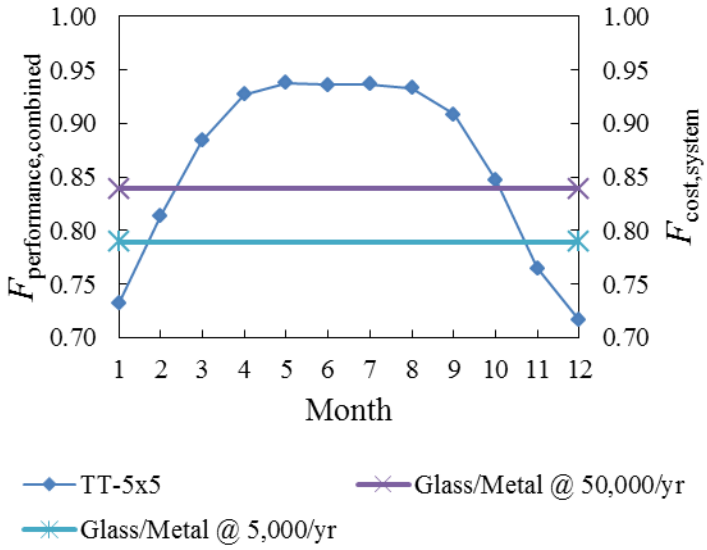

Fig. 56. Plot of cost factor (straight lines, right axis) and performance factor (curved lines, left axis) for 25-heliostat linkage simulations.

The results of Figs. 53–56 show that, under the specified assumptions, all except the TT-5x5 configuration sustain a performance factor above the capital cost factor for at least one of the heliostat cost models. It is interesting to note that the projected savings are greater for the smaller quantity (5,000/year). The reason for this is that higher quantities have a disproportionate impact on the cost due to the mirror compared to the drive. This means that the fraction of the overall cost devoted to the drive mechanism, and therefore potential for savings through linked tracking, is greater for smaller manufacturing quantities. This bodes well for a distributed-scale system, as fewer mirrors are used than in a typical large-scale tower plant. The analysis presented here is basic, and a more careful consideration of the load requirements and a more exhaustive economic analysis would be required to fully determine the best setup for a given application.

Chapter 7. Conclusions

A novel concentrating solar thermal power system using mechanically-linked heliostats and single and combined thermodynamic cycles has been analyzed. It is proposed that groups of heliostats within the field be mechanically linked, so as to move with the same relative velocity to one another during tracking. This approach provides the potential to save costs by reducing the number of tracking drives which make up a significant portion of the overall system cost, particularly for smaller heliostats. However, the linked tracking also introduces optical error. This work analyzes the effects of the linked tracking on system performance. It is found that the peak daily system efficiency when using a linked tracking system and single CO_2 Brayton cycle is 16.2% for a 1x2 heliostat linkage. The 1x2 linkage causes a maximum 1.64% reduction in system efficiency during December when compared to the case of individual tracking. A 5x5 linkage causes a 29.5% reduction in December system efficiency. When utilizing a CO_2–R-245fa combined cycle, the peak daily solar-to-electric conversion efficiency is calculated to be 18.2%.

This work has demonstrated the potential for utilizing a linked tracking mechanism in a distributed-scale power tower plant. Future work is suggested to implement a more rigorous receiver model, a mechanical analysis of the linkage design and performance, and a detailed economic analysis.

References

1. Sheldahl, Inc., 1974, "Summary of results of solar power arrays for the concentration of energy study," Report No. PB238003.
2. Trieb, F., 1999, "Competitive solar thermal power stations until 2010. The challenge of market introduction," J. Phys. IV France **9**, pp. 687–692.
3. Yao, Z., Wang, Z., Lu, Z., Wei, X., 2009, "Modeling and simulation of the pioneer 1 MW solar thermal central receiver system in China," Renewable Energy **34**, pp. 2437–2446.
4. Barlev, D., Vidu, R., Stroeve, P., 2011, "Innovation in concentrated solar power," Solar Energy Materials & Solar Cells **95**, pp. 2703–2725.
5. Goswami, D. Y., 1998, "Solar Thermal Power Technology: Present Status and Ideas for the Future," Energy Sources **20**, pp. 137–145.
6. Mills, D., 2004, "Advances in solar thermal electricity technology," Solar Energy **76**, pp. 19–31.
7. Price, H., Lupfert, E., Kearney, D., Zarza, D., Cohen, G., Gee, R., Mahoney, R., 2002, "Advances in Parabolic Trough Solar Power Technology," Journal of Solar Energy Engineering **124**, pp. 109–125.
8. Trieb, F., Langnib, O., and Klaib, H., 1997, "Solar electricity generation–A comparative view of technologies, costs and environmental impact," Solar Energy **59**(1–3), pp. 89–99.

9. Andraka, C. E., and Power, M. P., 2008, “Dish stirling development for utility-scale commercialization,” SolarPACES, Las Vegas, NV, USA. March 4–7, 2008.
10. Kolb, G.J., Alpert, D.J., Lopez, C.W., 1991, “Insights from the operation of Solar One and their implications for future central receiver plants,” Solar Energy **47**(1), pp. 39–47.
11. Ávila-Marín, A. L., 2011, “Volumetric receivers in Solar Thermal Power Plants with Central Receiver System technology: A review,” Solar Energy **85**, pp. 891–910.
12. Kribus, A., Doron, P., Rubin, R., Reuven, R., Taragan, E., Duchan, S., Karni, J., 2001, “Performance of the Directly-Irradiated Annular Pressurized Receiver (DIAPR) Operating at 20 Bar and 1,200°C,” Journal of Solar Energy Engineering **123**, pp. 10–17.
13. Becker, M., Fend, T., Hoffschmidt, B., Pitz-Paal, R., Reutter, O., Stamatov, V., Steven, M., and Trimis, D., 2006, “Theoretical and numerical investigation of flow stability in porous materials applied as volumetric solar receivers,” Solar Energy **80**, pp. 1241–1248.
14. Xu, C., Song, Z., Chen, L., and Zhen, Y., 2011, “Numerical investigation on porous media heat transfer in a solar tower receiver,” Renewable Energy **36**, pp. 1138–1144.

15. Moore, R., Vernon, M., Ho, C. K., Siegel, N. P., and Kolb, G. J., 2010, "Design Considerations for Concentrating Solar Power Tower Systems Employing Molten Salt," Sandia Report SAND2010–6978.
16. Forsberg, C. W., Peterson, P. F., and Zhao, H., 2007, "High-Temperature Liquid-Fluoride-Salt Closed-Brayton-Cycle Solar Power Towers," Journal of Solar Energy Engineering **129**, pp. 141–146.
17. Stine, W., Geyer, M., 2001, "Power From the Sun," from http://www.powerfromthesun.com/book.html.
18. Energy and Environmental Analysis, 2008, "Technology Characterization: Steam Turbines," Report prepared for Environmental Protection Agency, December 2008.
19. Schramek, P., Mills, D. R., Stein, W., Le Lievre, P., 2009, "Design of the Heliostat Field of the CSIRO Solar Tower," Journal of Solar Energy Engineering **131**, pp. 1–6.
20. Romero, M., Marcos, M. J., Tellez, F. M., Blanco, M., Fernandez, V., Baonza, F., Berger, S., 1999, "Distributed power from solar tower systems: A MIUS approach," Solar Energy **67**, pp. 249–264.
21. Göttsche, J., Hoffschmidt, Schmitz, S., Sauerborn, M., Buck, R., Teufel, E., Badstübner, K., Ifland, D., Rebholz, C., 2010, "Solar Concentrating Systems Using Small Mirror Arrays," Journal of Solar Energy Engineering **132**, Paper No. 011003.

22. Schell, S., 2011, “Design and evaluation of esolar’s heliostat fields,” Solar Energy **85**, pp. 614–619.
23. Kolb, G. J., Jones, S. A., Donnelly, M. W., Gorman, D., Thomas, R., Davenport, R., and Lumia, R., 2007, “Heliostat Cost Reduction Study,” Sandia Report SAND2007–3293.
24. Galanti, L., Massargo, A.F., 2011, “Micro gas turbine thermodynamic and economic analysis up to 500 kWe size,” Applied Energy **88**, pp. 4795–4263.
25. Vera, D., Jurado, F., de Mena, B., Schories, G., 2011, “Comparison between externally fired gas turbine and gasifier-gas turbine system for the olive oil industry,” Energy **36**(12), pp. 6720–6730.
26. Datta, A., Ganguly, R., Sarkar, L., 2010, “Energy and exergy analyses of an externally fired gas turbine (EFGT) cycle integrated with biomass gasifier for distributed power generation,” Energy **35**, pp. 341–350.
27. Craig, J.D., Purvis, C.R., 1999, “A Small Scale Biomass Fueled Gas Turbine Engine,” Transactions of the ASME **121**, pp. 64–67.
28. Garcia, P., Ferriere, A., Bezian, J., 2008, “Codes for solar flux calculation dedicated to central receiver system applications: A comparative review,” Solar Energy **82**, pp. 189–197.
29. Wei, X., Lu, Z., Yu, W., Wang, Z., 2010, “A new code for the design and analysis of the heliostat field layout for power tower system,” Solar Energy **84**, pp. 685–690.

30. Klein, S. A., 2012, Engineering Equation Solver (EES) for Microsoft Windows Operating System: Academic Professional Version, Madison, WI: F-Chart Software.
31. Duffie, J.A., Beckman, W.A., 2006, *Solar Engineering of Thermal Processes*, 3rd ed., John Wiley & Sons Hoboken, NJ.
32. Spencer, J.W., 1971, "Fourier Series Representation of the Position of the Sun," Search **2**(5), pp. 172.
33. Yang, B., Zhao, J., Xu, T., and Zhu, W., 2010, "Calculation of the Concentrated Flux Density Distribution in Parabolic Trough Solar Concentrators by Monte Carlo Ray-Trace Method," 2010 Symposium on Photonics and Optoelectronics.
34. Meinel, A., Meinel, M., 1976, *Applied Solar Energy, an introduction*, Reading, MA: Addison-Wesley.
35. Forero, N. L., Caicedo, L. M., Gordillo, G., 2007, "Correlation of global solar radiation values estimated and measured on an inclined surface for clear days in Bogotá," Renewable Energy **32**, pp. 2590–2602.
36. Kasten, F., Young, A., 1989, "Revised Optical Air Mass Tables and Approximation Formula," Applied Optics **28**.
37. Modest, M., 2003, *Radiative Heat Transfer*, 2nd ed., Academic Press, San Diego, CA.

38. Mousazadeh, H., Keyhani, A., Javadi, A., Mobli, H., Abrinia, K., Sharifi, A., 2009, "A review of principle and sun-tracking methods for maximizing solar systems output," Renewable and Sustainable Energy Reviews **13**, pp. 1800–1818.
39. Davis, J. M., Cotton, E. S., 1957, "Design of the quartermaster solar furnace," Solar Energy **1**(2–3), pp. 16–22.
40. Angelino, G., Invernizzi, C., Molteni, G., 1998, "The potential role of organic bottoming Rankine cycles in steam power stations," Proceedings of the Institution of Mechanical Engineers **213**(A), pp. 75–81.
41. Liu, B.T., Chien, K.H., Wang, C.C., 2004, "Effect of working fluids on organic Rankine cycle for waste heat recovery," Energy **29**, pp. 1207–1217.
42. Chacartegui, R., Sanchez, D., Jimenez-Espadafor, F., Munoz, A., Sanchez, T., 2008, "Analysis of intermediate temperature combined cycles with a carbon dioxide topping cycle," GT200851053, *Proceedings, ASME Turbo Expo 2008: Power for Land, Sea and Air*, Berlin, Germany.
43. Wu, S. Y., Xiao, L., and Li, Y. R., 2010, "A parabolic dish/AMTEC solar thermal power system and its performance evaluation," Applied Energy **87**, pp. 452–462.
44. Kribus, A., 2002, "A high-efficiency triple cycle for solar power generation," Solar Energy **72**(1), pp. 1–11.
45. Marrero, I. O., Lefsaker, A. M., Razani, A., Kim, K. J., 2002, "Second law analysis and optimization of a combined triple power cycle," Energy Conversion and Management **43**, pp. 557–573.

46. Wang, X. D., Zhao, L., Wang, J. L., Zhang, W. Z., Zhao, X. Z., and Wu, W., 2010, "Performance evaluation of a low-temperature solar Rankine cycle system utilizing R245fa," Solar Energy **84**, pp. 353–364.
47. Abbas, M., Boumeddane, B., Said, N., Chikouche, A., 2011, "Stirling technology: A 100 MW solar power plant using hydrogen for Algeria," International Journal of Hydrogen Energy **36**, pp. 4305–4314.
48. Lemmon, E. W., Jacobsen, R. T., Penoncello, S. G., Friend, D., 2000, "Thermodynamic Properties of Air and Mixtures of Nitrogen, Argon, and Oxygen from 60 to 2000 K at Pressures to 2000 MPa," Journal of Physical and Chemical Reference Data **29**(3), pp. 331–385.
49. Span, R., Wagner, W., 1996, "A New Equation of State for Carbon Dioxide Covering the Fluid Region from the Triple-Point Temperature to 1100 K at Pressures up to 800 MPa," Journal of Physical and Chemical Reference Data **25**(6), pp. 1509–1596.
50. McCarty, R. D., Ap, V. D., 1990, "A New Wide Range Equation of State for Helium," Advances in Cryogenic Engineering **35**, pp. 1465–1475.
51. Leachman, J. W., Jacobsen, R. T., Penoncello, S. G., and Lemmon, E. W., 2009, "Fundamental Equations of State for Parahydrogen, Normal Hydrogen, and Orthohydrogen," Journal of Physical Chemical and Reference Data **38**, 721.

52. Penoncello, S.G., Jacobsen, R. T., and Goodwin, A. R. H., 1995, “A Thermodynamic Property Formulation for Cyclohexane,” International Journal of Thermophysics **16**(2), pp. 519–529.

53. Jacobsen, R.T., Penoncello, S.G., and Lemmon, E.W., 1997, *Thermodynamic Properties of Cryogenic Fluids*, Plenum Press, New York.

54. Martin, J. J., and Hou, Y. C., 1955, “Development of An Equation of State for Gases,” AIChE Journal **1**(142), pp. 142–151.

55. Lemmon, E. W., and Span, R., 2006, “Short Fundamental Equations of State for 20 Industrial Fluids,” Journal of Chemical & Engineering Data **51**(3), pp. 785–850.